Article

B cells are associated with survival and immunotherapy response in sarcoma

https://doi.org/10.1038/s41586-019-1906-8

Received: 29 June 2018

Accepted: 26 November 2019

Published online: 15 January 2020

Florent Petitprez[1,2,3,4], Aurélien de Reyniès[4,24], Emily Z. Keung[5,24], Tom Wei-Wu Chen[6,7,8,9], Cheng-Ming Sun[1,2,3], Julien Calderaro[1,10,11], Yung-Ming Jeng[9,12], Li-Ping Hsiao[7], Laetitia Lacroix[1,2,3], Antoine Bougoüin[1,2,3], Marco Moreira[1,2,3], Guillaume Lacroix[1,2,3], Ivo Natario[1,2,3], Julien Adam[13], Carlo Lucchesi[14,15], Yec'han Laizet[14,15], Maud Toulmonde[14,16], Melissa A. Burgess[17], Vanessa Bolejack[18], Denise Reinke[19], Khalid M. Wani[20], Wei-Lien Wang[20], Alexander J. Lazar[20,21], Christina L. Roland[5], Jennifer A. Wargo[5,21], Antoine Italiano[14,16,22], Catherine Sautès-Fridman[1,2,3], Hussein A. Tawbi[23]* & Wolf H. Fridman[1,2,3]*

Soft-tissue sarcomas represent a heterogeneous group of cancer, with more than 50 histological subtypes[1,2]. The clinical presentation of patients with different subtypes is often atypical, and responses to therapies such as immune checkpoint blockade vary widely[3,4]. To explain this clinical variability, here we study gene expression profiles in 608 tumours across subtypes of soft-tissue sarcoma. We establish an immune-based classification on the basis of the composition of the tumour microenvironment and identify five distinct phenotypes: immune-low (A and B), immune-high (D and E), and highly vascularized (C) groups. In situ analysis of an independent validation cohort shows that class E was characterized by the presence of tertiary lymphoid structures that contain T cells and follicular dendritic cells and are particularly rich in B cells. B cells are the strongest prognostic factor even in the context of high or low $CD8^+$ T cells and cytotoxic contents. The class-E group demonstrated improved survival and a high response rate to PD1 blockade with pembrolizumab in a phase 2 clinical trial. Together, this work confirms the immune subtypes in patients with soft-tissue sarcoma, and unravels the potential of B-cell-rich tertiary lymphoid structures to guide clinical decision-making and treatments, which could have broader applications in other diseases.

Soft-tissue sarcomas (STSs) comprise many histological subtypes with distinct clinical and biological behaviours. Genetically 'simple' STSs are characterized by translocations that result in fusion proteins and few, if any, other genomic lesions, whereas 'complex' STSs have an unbalanced karyotype and several genomic aberrations[1]. STSs are considered 'non-immunogenic' with a low mutational burden[2]. Among complex tumours, undifferentiated pleomorphic sarcoma (UPS), dedifferentiated liposarcoma (DDLPS) and—to a lesser extent—leiomyosarcoma (LMS) can exhibit durable responses to immune-checkpoint blockade, whereas simple tumours do not respond to PD1 monotherapy or a combination of anti-PD1 and anti-CTLA4 antibodies[3,4]. Few reports investigating the composition of the tumour microenvironment (TME) in different STS histologies have been published[5–7], but a recent study from The Cancer Genome Atlas (TCGA) consortium suggested an association with prognosis[8].

Here, we developed a new classification of STS, based on the composition of the TME in large cohorts of STS, using the microenvironment cell populations (MCP)-counter method[9]. We found that the B lineage signature—a hallmark of an immune-high class we called E—correlated with an improved survival of patients with STS, in tumours with both high or low infiltration of $CD8^+$ T cells. In an independent cohort, we used immunohistochemistry to validate the high density of B cells and presence of tertiary lymphoid structures (TLS) in class E. Finally, we showed that class E exhibited the highest response rate to PD1 blockade therapy and improved progression-free survival in a multicentre phase 2 clinical trial of pembrolizumab in STS (SARC028)[4,10].

[1]Team Cancer, Immune Control and Escape, Centre de Recherche des Cordeliers, INSERM, Paris, France. [2]Centre de Recherche des Cordeliers, Université de Paris, Sorbonne Paris Cite, Paris, France. [3]Centre de Recherche des Cordeliers, Sorbonne University, Paris, France. [4]Programme Cartes d'Identité des Tumeurs, Ligue Nationale Contre le Cancer, Paris, France. [5]Department of Surgical Oncology, The University of Texas MD Anderson Cancer Center, Houston, TX, USA. [6]Graduate Institute of Oncology, National Taiwan University College of Medicine, Taipei, Taiwan. [7]Department of Oncology, National Taiwan University Hospital, Taipei, Taiwan. [8]National Taiwan University Cancer Center, Taipei, Taiwan. [9]Centers of Genomic and Precision Medicine, National Taiwan University, Taipei, Taiwan. [10]Département de Pathologie, Assistance Publique Hôpitaux de Paris, Groupe Hospitalier Henri Mondor, Creteil, France. [11]Institut Mondor de Recherche Biomédicale, Creteil, France. [12]Department of Pathology, National Taiwan University, Taipei, Taiwan. [13]Department of Biology and Pathology, Gustave Roussy, Villejuif, France. [14]Institut Bergonié, Bordeaux, France. [15]Bioinformatics Unit, Institut Bergonié, Bordeaux, France. [16]Department of Medical Oncology, Institut Bergonié, Bordeaux, France. [17]Department of Medicine, Divison of Hematology/Oncology, University of Pittsburgh, Pittsburgh, PA, USA. [18]Cancer Research and Biostatistics, Seattle, WA, USA. [19]Sarcoma Alliance for Research Through Collaboration, Ann Arbor, MI, USA. [20]Department of Pathology, The University of Texas MD Anderson Cancer Center, Houston, TX, USA. [21]Department of Genomic Medicine, The University of Texas MD Anderson Cancer Center, Houston, TX, USA. [22]University of Bordeaux, Bordeaux, France. [23]Department of Medical Oncology, The University of Texas MD Anderson Cancer Center, Houston, TX, USA. [24]These authors contributed equally: A. de Reyniès, E. Z. Keung. *e-mail: htawbi@mdanderson.org; herve.fridman@crc.jussieu.fr

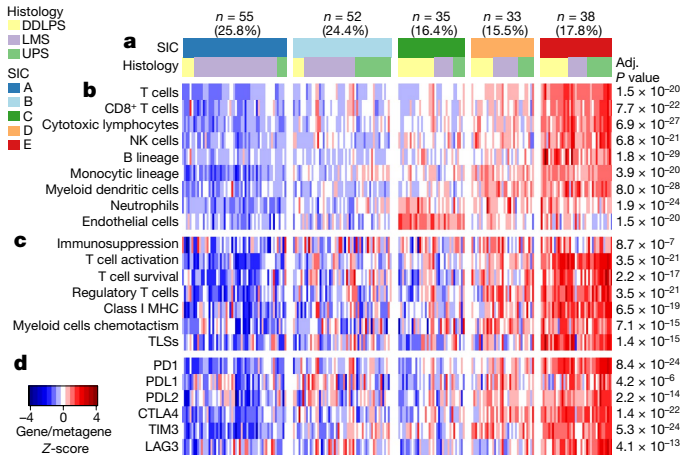

Fig. 1 | The SICs exhibit strongly different TMEs. This figure refers to the TCGA SARC cohort ($n = 213$). **a**, Composition of the TCGA SARC cohort by SIC, and histology. **b**, Composition of the TME by SIC as defined by the MCP-counter *Z*-scores. NK cells, natural killer cells. **c**, Expression of gene signatures related to the functional orientation of the immune TME by SIC. **d**, Expression of genes related to immune checkpoints by SIC. Adjusted *P* values are obtained from Benjamini–Hochberg correction of two-sided Kruskal–Wallis tests *P* values.

Immune classification of STS

The TME compositions from four independent discovery primary STS datasets (TCGA SARC, Gene Expression Omnibus (GEO) accessions GSE21050, GSE21122 and GSE30929) (Extended Data Table 1) with publicly available gene expression profiles were analysed by MCP-counter, a gene-expression-based TME deconvolution tool[9]. An immune-based classification of STS was developed from this analysis (Extended Data Fig. 1, Methods) and tumours were assigned to one of five sarcoma immune classes (SICs), labelled A, B, C, D and E, with highly distinct profiles (Fig. 1).

We compared the SIC distribution across histological subtypes and found that most LMS tumours were classified to SICs A and B (Fig. 1a). DDLPS accounted for half of SIC C tumours. Tumours classified as SICs D and E were more evenly distributed across histological subtypes. Application of the predictor of the immune classes (Methods) to other STS histologies from French Sarcoma Group (FSG) cohort (Extended Data Table 1) revealed that all SICs could be identified in each histology (Extended Data Fig. 2a).

The TME composition differs significantly between SICs (Fig. 1b). Three SICs showed homogeneous profiles. SIC A, 'immune desert', was characterized by the lowest expression of gene signatures related to immune cells, as well as low vasculature. SIC C, 'vascularized', was dominated by a high expression of endothelial-cell-related genes. SIC E, 'immune and TLS high', was characterized by the highest expression of genes specific to immune populations such as T cells, $CD8^+$ T cells, natural killer cells and cytotoxic lymphocytes. Notably, a key determinant of SIC E was the high expression of the B lineage signature ($P = 1.8 \times 10^{-29}$). SICs B and D were characterized by heterogeneous but generally immune-low and immune-high profiles, respectively.

The expression of genes associated with T cell or myeloid cell chemotaxis, T cell activation and survival, major histocompatibility complex class I, and regulatory gene signatures was high in SICs D and E, intermediate in SICs B and C, and very low in SIC A (Fig. 1c). Expression of the lymphoid-structures-associated B-cell-specific chemokine CXCL13 was notably high in E tumours, moderate in D tumours, generally low in B and C tumours, and negligible in A tumours.

The expression of immune-checkpoint-related genes (Fig. 1d) followed that of immune infiltrates, with high expression of the genes encoding PD1, PDL2, CTLA4 and TIM3 (*PDCD1*, *PDCD1LG2*, *CTLA4* and *HAVCR2*, respectively) in SIC E followed by SIC D tumours, and low-to-very-low expression in SIC C, B and A tumours. *CD274* (which encodes PDL1) was heterogeneously expressed across SICs, whereas *LAG3* was expressed at high levels only in SIC E tumours, and its expression was low in all other classes. The above findings were consistent across the four discovery cohorts (Extended Data Fig. 3).

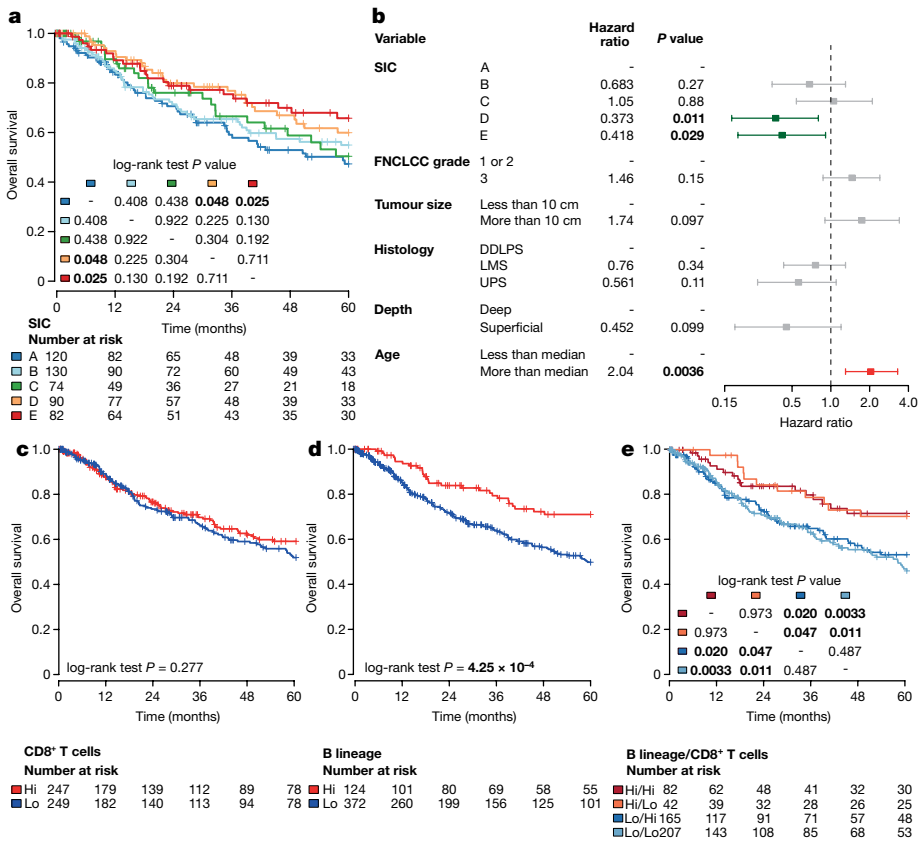

Fig. 2 | SICs and B cells are predictive of the survival of patients with STS. This figure refers to TCGA SARC and GSE21050 pooled cohorts ($n = 496$). **a**, Overall survival of patients with STS by the SIC of their tumour. **b**, Multivariate Cox proportional regression outcome, with all included variables represented. For each variable, the reference level is the first one. A grey bar indicates $P > 0.05$; and variables indicated by green and red bars are positively and negatively, respectively, significantly associated with prognosis in this multivariate model. Error bars represent the 95% confidence interval. FNCLCC, Fédération Nationale des Centres de Lutte Contre le Cancer. **c**, **d**, Overall survival of patients with STS according to MCP-counter scores for $CD8^+$ T cells (**c**) or B lineage cells (**d**). **e**, Overall survival of patients based on the tumour-infiltrating B lineage cells and $CD8^+$ T cells. Analyses were performed with Kaplan–Meier estimates and two-sided log-rank tests. In each cohort, tumours were considered high (Hi) for $CD8^+$ T cells if their score was above the median, and high for cytotoxic lymphocytes and B lineage if their score was above the third quartile.

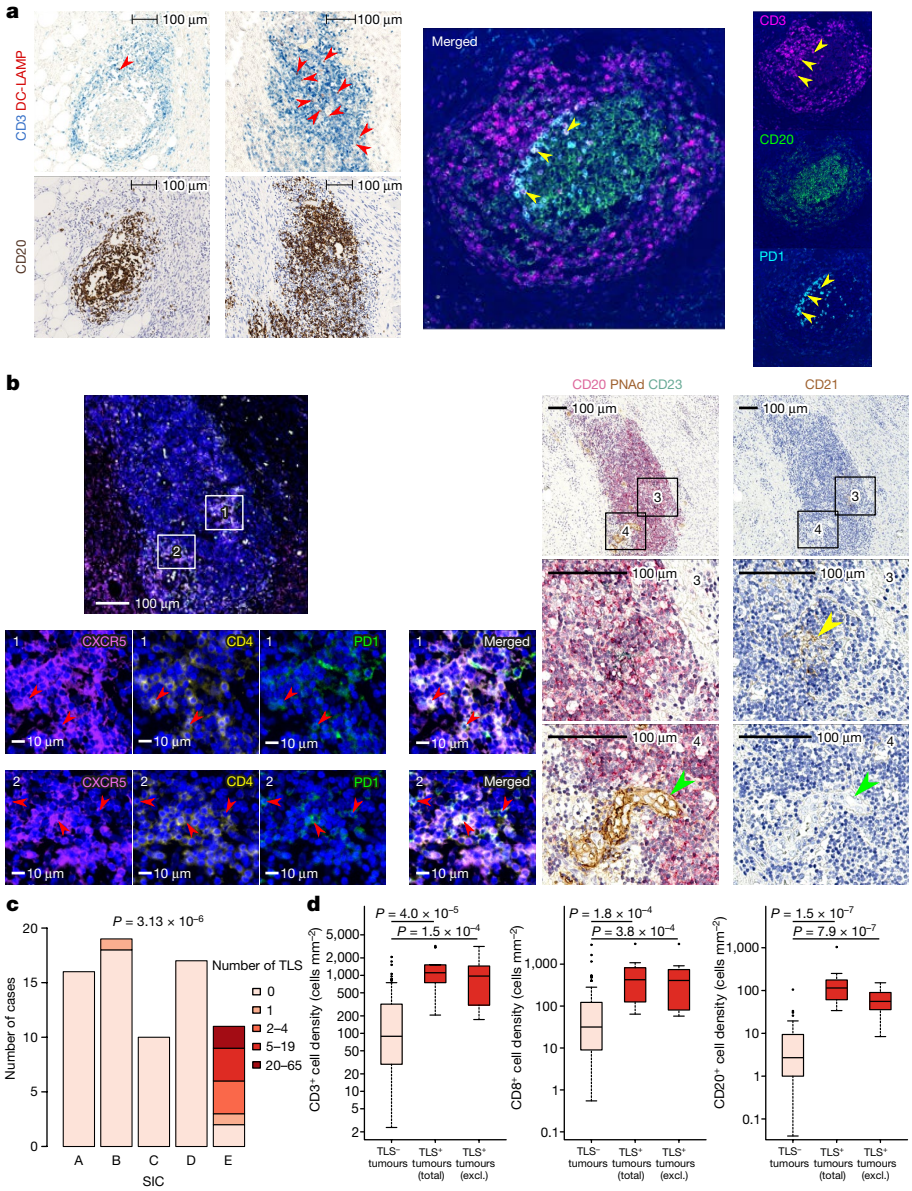

Fig. 3 | TLSs are a distinguishing feature of the immune-high class of STS. This figure refers to the NTUH cohort ($n = 93$). **a**, Populational characterization of TLSs. Left, examples of two tertiary lymphoid structures by immunohistochemistry, identified as $CD3^+$ T cell (blue) aggregates containing DC-$LAMP^+$ mature dendritic cells (red, red arrows) and juxtaposing $CD20^+$ B cell aggregates (brown). Right, representative immunofluorescence staining of a TLS for CD3 (magenta), CD20 (green) and PD1 (cyan). DAPI staining is shown in blue. The multispectral image shows $CD3^+PD1^+$ double-positive cells (yellow arrows). **b**, Functionality of TLSs. Left, $CXCR5^+$ (magenta), $CD4^+$ (yellow) and $PD1^+$ (green) cells in zones 1 and 2 of the same TLS. Multispectral fluorescence images of zones 1 and 2 show $CXCR5^+CD4^+PD1^+$ triple positive cells (red arrows) characteristic of T follicular helper cells. Right, $CD20^+$ cells stained in pink (left) on consecutive sections of a TLS. CD23 (green on left) and CD21 (brown on right) positive cells with reticular morphology characteristic of follicular dendritic cells (yellow arrow, zone 3). $PNAd^+$ structures (brown, green arrow) with high endothelial venule morphology are also detectable nearby (zone 4). **c**, Number of TLS among 5 SICs of 73 tumours of NTUH cohort ($n = 73$). **d**, Characterization of the immune infiltrate in tumours according to TLS presence (TLS^- $n = 82$, TLS^+ $n = 11$, total $n = 93$). Densities of $CD3^+$ (left), $CD8^+$ (centre) and $CD20^+$ (right) cells in tumours lacking or containing TLSs; densities including (total) or excluding (excl) TLS are indicated for the TLS^+ tumours. Box plots represent median (larger bar) and interquartile range (IQR). Upper whisker extends to whichever is minimal, maximum or third quartile plus 1.5× IQR. Lower whisker extends to whichever is maximal, minimum or first quartile minus 1.5× IQR. *P* values were determined by chi-squared test (**c**) or two-sided Mann–Whitney tests (**d**).

SICs are associated with patient survival

After confirmation that the two cohorts with available survival data (TCGA SARC, $n = 213$; GSE21050, $n = 283$) exhibited similar survival patterns (data not shown), the cohorts were pooled to study the clinical outcome of the five SICs (Fig. 2a). Patients with SIC A exhibited the shortest overall survival compared with group D or E patients ($P = 0.048$ and $P = 0.025$, respectively). Similarly, among the other STS histologies from the FSG cohort, patients with SIC A had a shorter overall survival than patients with SIC E (Extended Data Fig. 2b). In a multivariate model with classical prognostic factors (Fig. 2b), SICs were found to be significantly associated with prognosis, independent of other clinical parameters (as compared with SIC A; $P = 0.011$ and $P = 0.029$, for SICs D and E, respectively). Tumours were separated between high and low expression of $CD8^+$ T cells, cytotoxic lymphocytes and B lineage signatures based on the observation of the MCP-counter scores distribution (Extended Data Fig. 4). Detailed analysis of the effect of these immune cell population signatures revealed that whereas neither $CD8^+$ T cells ($P = 0.277$) (Fig. 2c) nor cytotoxic lymphocytes ($P = 0.0513$) (Extended Data

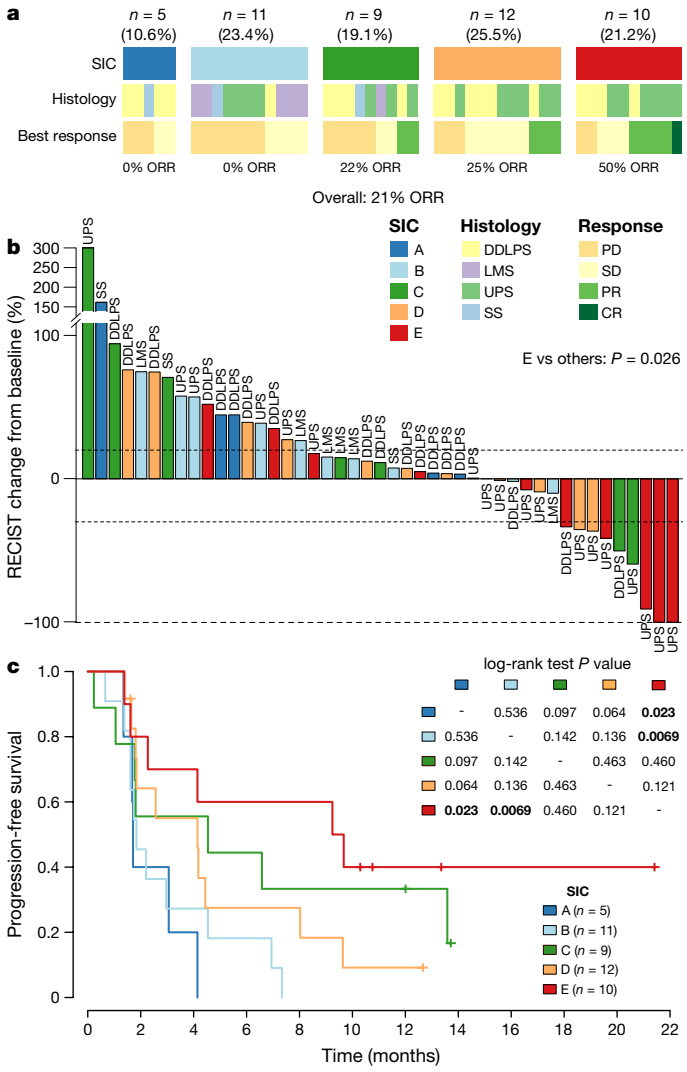

Fig. 4 | SICs are strongly associated with STS response to PD1 blockade therapy. This figure refers to the SARC028 cohort ($n = 47$). **a**, Relationship between SIC, histology and response to treatment in the SARC028 cohort. **b**, Waterfall plot showing the best response to pembrolizumab as a percentage change in the size of target lesions from baseline ($n = 45$). Tumour sizes were calculated as the sum of target lesion diameters. Colours indicate the SIC to which each tumour was assigned. Dashed lines indicate +20%, −30% and −100% change from baseline levels. SIC E versus other comparison was performed using a two-sided Mann–Whitney test. CR, complete response; PD, progressive disease; PR, partial response; SD, stable disease; SS, synovial sarcoma. **c**, Progression-free survival of patients by tumour SIC ($n = 47$).

Fig. 5a) significantly correlated with survival, the B lineage signature was significantly associated with improved overall survival ($P = 4.25 \times 10^{-4}$) (Fig. 2d). When analysed in the context of high or low infiltration of CD8$^+$ T cells (Fig. 2e), cytotoxic lymphocytes or the expression of *PDCD1* (PD1), *CD274* (PDL1) or *FOXP3* (Extended Data Fig. 5b–e), the B lineage signature was the dominant parameter for improved survival, regardless of the expression of other immune factors. In addition, SIC E tumours demonstrate high expression of both *IGJ* (also known as *JCHAIN*) and *TNFRSF17* (encoding BCMA) (data not shown), which indicates that plasma cells[11] may contribute to improved prognosis.

Mutational landscape of SICs in TCGA SARC

The overall tumour mutational burden was low across the studied cohorts (median: 32 non-synonymous mutations) and appeared to be similar across all SICs (Extended Data Fig. 6a). However, a few highly mutated tumours (each with more than 250 non-synonymous mutations) were found in the D and E groups. Qualitative mutational analysis revealed several commonly mutated genes across the cohort, including *TP53* (35.2%), *ATRX* (16.0%), *TTN* (9.9%), *RB1* (8.9%), *MUC16* (8.0%), *PCLO* (6.1%), *DNAH5*, *MUC17* and *USH2A* (5.2% each) (Extended Data Fig. 6b). *TP53* was more frequently mutated among SICs D and E tumours ($P = 0.01$) (Extended Data Fig. 6c).

The landscape of copy-number variations, assessed on the TCGA SARC cohort, revealed differences between histologies, consistent with previous observations[8]. However, there was no notable difference in copy-number variation between SICs (data not shown).

In situ validation of SIC profiles in tumours

To validate the TME profiles of SICs in situ, we analysed an independent cohort of 93 STS cases (NTUH cohort) (Extended Data Table 1). Seventy-three samples passed quality control for transcriptomic analysis using Nanostring nCounter technology. We classified this cohort into the same five SICs (Methods) with the following distribution: A, 16 (21.9%); B, 19 (26.0%); C, 10 (13.7%); D, 17 (23.3%); and E, 11 (15.1%). The NTUH cohort samples exhibited gene-expression-based TME profiles that were similar to that of TCGA SARC and GSE21050 cohorts (Extended Data Fig. 7a).

By quantitative immunohistochemistry, immune-desert SIC A was characterized by very low densities of CD3$^+$, CD8$^+$ or CD20$^+$ cells, whereas immune-and-TLS-high SIC E exhibited high densities of these cells (pairwise comparison, $P = 4.01 \times 10^{-6}$, $P = 6.64 \times 10^{-6}$ and $P = 9.90 \times 10^{-7}$, respectively). The vascularized SIC C exhibited a moderate infiltration by immune cells and a high density of CD34$^+$ endothelial cells (Extended Data Fig. 7b, c).

TLSs are a feature of SIC E tumours

The CXCL13 chemokine, which is associated with the presence of TLSs[12], was strongly expressed in SIC E tumours (Fig. 1c, Extended Data Fig. 2c). Expression of CXCL13 was highly correlated with that of the TLS-associated 12-chemokine signature[13] (Extended Data Fig. 8a), which suggests that TLSs could be a marker of SIC E. TLSs were defined as a CD20$^+$ B-cell follicle juxtaposed to a CD3$^+$ T cell aggregate containing at least one DC-LAMP$^+$ (also known as LAMP3$^+$) mature dendritic cell[12,14–16] (Fig. 3a, left). A strong association between SICs and the presence of TLSs was identified ($P = 3.13 \times 10^{-6}$) (Fig. 3c). No TLSs were observed in tumours from SICs A, C and D, and only one tumour from SIC B had one TLS. By contrast, nine out of eleven (82%) SIC E tumours exhibited one or more TLS. All TLSs were intratumoural (Extended Data Fig. 8b), and found at the periphery and in the centre of the tumour in all histologies (Extended Data Fig. 8c, d).

We observed the presence of CD3$^+$PD1$^+$ T cells (Fig. 3a, right) in the germinal centre of TLSs with characteristics of follicular T helper cells[17,18] (positive for CD4, PD1 and the CXCL13 receptor CXCR5) (Fig. 3b, left), CD23$^+$CD21$^+$ cells with reticular morphology characteristic of follicular dendritic cells, and peripheral node addressin (PNAd)-positive structures with high endothelial venules morphology (Fig. 3b, right). Germinal centres are a hallmark of secondary follicle-like TLSs (SFL-TLS), the final maturation step of TLS; the earlier steps being early TLSs (E-TLS) and primary follicle-like TLSs (PFL-TLS)[15,16]. E-TLS, PFL-TLS and SFL-TLS represented 60.5%, 21.1% and 18.3%, respectively, of all TLSs analysed (Extended Data Fig. 8e, f). This differed between histologies ($P = 7.76 \times 10^{-5}$), with UPS having only 16.7% of E-TLS.

Tumours with TLSs (11.8%, 11 out of 93) had significantly higher densities of tumour-infiltrating CD3$^+$ T cells ($P = 4.0 \times 10^{-5}$), CD8$^+$ T cells ($P = 1.8 \times 10^{-4}$) and CD20$^+$ B cells ($P = 1.5 \times 10^{-5}$) (Fig. 3d). This association persisted even if T and B cells within TLSs were excluded from the analysis ($P = 1.5 \times 10^{-4}$, $P = 3.8 \times 10^{-4}$ and $P = 7.9 \times 10^{-7}$, respectively) (Fig. 3d), which suggests that high immune cell infiltration is not limited to TLSs.

SICs predict patient response to PD1 blockade

We examined whether SICs can predict the patient response to checkpoint blockade therapy. We obtained 47 pre-treatment STS metastasis biopsies from patients enrolled in the SARC028 clinical trial[4] and its expansion cohort[10] (Extended Data Table 1), which evaluated the efficacy of the anti-PD1 monoclonal antibody pembrolizumab in patients with metastatic STS. Of these 47 patients, 1 achieved a complete response, 9 a partial response, 17 stable disease and 20 had progressive disease (Fig. 4a). Pre-treatment tumours were classified into SICs based on gene-expression data. The objective response rate (ORR) (which accounts for complete and partial responses) as evaluated by response evaluation criteria in solid tumours (RECIST) criteria was 21.2% in the overall cohort. SICs, however, showed substantial variation in ORR, with SIC E patients exhibiting the highest ORR (50%, 5 out of 10), followed by SIC D (25%, 3 out of 12) and SIC C (22%, 2 out of 9) (Fig. 4a). A complete response was found only in SIC E, as well as one patient who had a 100% change in target lesions but a non-complete response in non-target lesions and thus did not qualify for a complete response. Notably, there were no responders within the SIC A (0 out of 5) and B (0 out of 11) groups (Fig. 4a). Overall, SIC E tumours were associated with the highest response rate to pembrolizumab in comparison with tumours from other SICs ($P = 0.026$, Fig. 4b). Patients with SIC E tumours also exhibited improved progression-free survival compared with patients with SIC A or B tumours ($P = 0.023$ and $P = 0.0069$, respectively) (Fig. 4c).

Discussion

This study is, to our knowledge, the most comprehensive analysis of the STS immune TME and the first to evaluate the prognostic effect of immune infiltrates by simultaneously integrating several immune cell populations and malignant cell characteristics. Previous studies have examined the immune profile of STS tumours, but the importance of B cells and TLSs was not investigated. The clinical effect of $CD8^+$ T cells and PD1 expression has yielded controversial results[7,8,19–25]. Here, we found the $CD8^+$ T cell signature and PD1 were expressed in class D and E SICs, which are associated with favourable outcomes, providing high infiltration of B cells. The integrative analysis demonstrates that infiltration by B cells is a key discriminative feature of a group of patients with improved survival. This B-cell-high group was found to respond better to PD1 blockade therapy, although this should be validated on a larger cohort.

The field of immuno-oncology is rapidly expanding, and is crucial to accurately identify patients who are likely to respond. Here, we propose a classification for STS that is immune-centric with prognostic effect. It defines a group of patients with a better response to anti-PD1 therapy marked by B cells and TLSs. This finding may have broad applications. Sarcomas are considered immune-quiescent tumours, with a low mutational burden. Nevertheless, our data show that some STSs are immunogenic and that this is driven by B cells. Further work is needed to extend these findings to all STS histologies and other cancers. Similarly, the underlying mechanisms require further investigation, but a possible explanation is that TLSs are sites at which anti-tumoral immunity is generated, with B cells instructing T cells—in particular $CD8^+$ T cells—to recognize tumour-associated antigens[26]. It is noteworthy that TLS-rich tumours are more infiltrated by $CD8^+$ T cells. These T cells can become exhausted, explaining the correlation of the expression of immune checkpoints (such as PD1 and LAG3) with TLSs, and why treatment with checkpoint inhibitors may allow productive anti-tumour immunity in TLS-rich tumours. Overall, our findings lay the foundation for a tool to risk-stratify patients with STS and identify those who may be more likely to benefit from immunotherapies, and may be broadly applicable to other malignancies[26–30].

Online content

Any methods, additional references, Nature Research reporting summaries, source data, extended data, supplementary information, acknowledgements, peer review information; details of author contributions and competing interests; and statements of data and code availability are available at https://doi.org/10.1038/s41586-019-1906-8.

1. Helman, L. J. & Meltzer, P. Mechanisms of sarcoma development. *Nat. Rev. Cancer* **3**, 685–694 (2003).
2. Fletcher, C., Bridge, J., Hogendoorn, P. & Mertens, F. *WHO Classification of Tumours of Soft Tissue and Bone* (World Health Organization, 2013).
3. D'Angelo, S. P. et al. Nivolumab with or without ipilimumab treatment for metastatic sarcoma (Alliance A091401): two open-label, non-comparative, randomised, phase 2 trials. *Lancet Oncol.* **19**, 416–426 (2018).
4. Tawbi, H. A. et al. Pembrolizumab in advanced soft-tissue sarcoma and bone sarcoma (SARC028): a multicentre, two-cohort, single-arm, open-label, phase 2 trial. *Lancet Oncol.* **18**, 1493–1501 (2017).
5. Beck, A. H. et al. Discovery of molecular subtypes in leiomyosarcoma through integrative molecular profiling. *Oncogene* **29**, 845–854 (2010).
6. Gibault, L. et al. New insights in sarcoma oncogenesis: a comprehensive analysis of a large series of 160 soft tissue sarcomas with complex genomics. *J. Pathol.* **223**, 64–71 (2011).
7. Pollack, S. M. et al. T-cell infiltration and clonality correlate with programmed cell death protein 1 and programmed death-ligand 1 expression in patients with soft tissue sarcomas. *Cancer* **123**, 3291–3304 (2017).
8. Cancer Genome Atlas Research Network. Comprehensive and integrated genomic characterization of adult soft tissue sarcomas. *Cell* **171**, 950–965.e28 (2017).
9. Becht, E. et al. Estimating the population abundance of tissue-infiltrating immune and stromal cell populations using gene expression. *Genome Biol.* **17**, 218 (2016).
10. Burgess, M. A. et al. Clinical activity of pembrolizumab (P) in undifferentiated pleomorphic sarcoma (UPS) and dedifferentiated/pleomorphic liposarcoma (LPS): final results of SARC028 expansion cohorts. *JCO* **37**, 11015–11015 (2019).
11. Kroeger, D., Milne, K. & H Nelson, B. Tumor-infiltrating plasma cells are associated with tertiary lymphoid structures, cytolytic T-cell responses, and superior prognosis in ovarian cancer. *Clinical Cancer Res.* **22**, 3005–3015 (2016).
12. Sautès-Fridman, C., Petitprez, F., Calderaro, J. & Fridman, W. H. Tertiary lymphoid structures in the era of cancer immunotherapy. *Nat. Rev. Cancer* **19**, 307–325 (2019).
13. Coppola, D. et al. Unique ectopic lymph node-like structures present in human primary colorectal carcinoma are identified by immune gene array profiling. *Am. J. Pathol.* **179**, 37–45 (2011).
14. Dieu-Nosjean, M.-C., Goc, J., Giraldo, N. A., Sautès-Fridman, C. & Fridman, W. H. Tertiary lymphoid structures in cancer and beyond. *Trends Immunol.* **35**, 571–580 (2014).
15. Posch, F. et al. Maturation of tertiary lymphoid structures and recurrence of stage II and III colorectal cancer. *OncoImmunology* **7**, e1378844 (2017).
16. Siliņa, K. et al. Germinal centers determine the prognostic relevance of tertiary lymphoid structures and are impaired by corticosteroids in lung squamous cell carcinoma. *Cancer Res.* **78**, 1308–1320 (2018).
17. Gu-Trantien, C. et al. $CD4^+$ follicular helper T cell infiltration predicts breast cancer survival. *J. Clin. Invest.* **123**, 2873–2892 (2013).
18. Dorfman, D. M., Brown, J. A., Shahsafaei, A. & Freeman, G. J. Programmed death-1 (PD-1) is a marker of germinal center-associated T cells and angioimmunoblastic T-cell lymphoma. *Am. J. Surg. Pathol.* **30**, 802–810 (2006).
19. D'Angelo, S. P. et al. Prevalence of tumor-infiltrating lymphocytes and PD-L1 expression in the soft tissue sarcoma microenvironment. *Hum. Pathol.* **46**, 357–365 (2015).
20. Sorbye, S. W. et al. Prognostic impact of peritumoral lymphocyte infiltration in soft tissue sarcomas. *BMC Clin. Pathol.* **12**, 5 (2012).
21. Sorbye, S. W. et al. High expression of $CD20^+$ lymphocytes in soft tissue sarcomas is a positive prognostic indicator. *OncoImmunology* **1**, 75–77 (2012).
22. Bertucci, F. et al. PDL1 expression is a poor-prognosis factor in soft-tissue sarcomas. *OncoImmunology* **6**, e1278100 (2017).
23. Kim, J. R. et al. Tumor infiltrating PD1-positive lymphocytes and the expression of PD-L1 predict poor prognosis of soft tissue sarcomas. *PLoS One* **8**, e82870 (2013).
24. Honda, Y. et al. Infiltration of PD-1-positive cells in combination with tumor site PD-L1 expression is a positive prognostic factor in cutaneous angiosarcoma. *OncoImmunology* **6**, e1253657 (2016).
25. Paydas, S., Bagir, E. K., Deveci, M. A. & Gonlusen, G. Clinical and prognostic significance of PD-1 and PD-L1 expression in sarcomas. *Med. Oncol.* **33**, 93 (2016).
26. Nielsen, J. S. et al. $CD20^+$ tumor-infiltrating lymphocytes have an atypical CD27- memory phenotype and together with $CD8^+$ T cells promote favorable prognosis in ovarian cancer. *Clin. Cancer Res.* **18**, 3281–3292 (2012).
27. Montfort, A. et al. A strong B-cell response is part of the immune landscape in human high-grade serous ovarian metastases. *Clin. Cancer Res.* **23**, 250–262 (2017).
28. Hennequin, A. et al. Tumor infiltration by $Tbet^+$ effector T cells and $CD20^+$ B cells is associated with survival in gastric cancer patients. *OncoImmunology* **5**, e1054598 (2015).
29. Wouters, M. C. A. & Nelson, B. H. Prognostic significance of tumor-infiltrating B cells and plasma cells in human cancer. *Clin. Cancer Res.* **24**, 6125–6135 (2018).
30. Helmink, B. et al. B cells and tertiary lymphoid structures promote immunotherapy response. *Nature* https://doi.org/10.1038/s41586-019-1922-8 (2020).

Methods

Ethics and patients

Patients diagnosed with DDLPS, LMS and UPS were identified and the pathology diagnosis was confirmed by a certified pathologist in National Taiwan University Hospital. The research was approved by the Research Ethics Committee of NTUH (201605061RINA) for this retrospective study. Formalin-fixed paraffin-embedded (FFPE) blocks were retrieved and 4–5-µm-thick slides were taken for immunohistochemistry staining and RNA extraction for Nanostring testing. Other cohorts were previously published[4,8,31–35].

Establishing the immune classification of STS

To establish a robust immune classification of STS, publicly available transcriptomic data from TCGA data portal and the GEO repository representing four large and independent patient cohorts were included. Only tumours from the most common histologies of genomically complex STS were included: LMS, UPS and DDLPS. We analysed data from the TCGA SARC[8] ($n = 213$), GSE21050[31] ($n = 283$), GSE21122[32] ($n = 72$) and GSE30929[33] ($n = 40$) cohorts.

Public transcriptomic data pre-processing

Transcriptomic data were downloaded from the TCGA data portal (SARC cohort) and GEO (accessions GSE21050, GSE21122 and GSE30929). TCGA SARC was restricted to complex genomics sarcomas (UPS, DDLPS and LMS). Normalized TCGA SARC RNA-sequencing data were $\log_2$-transformed. Microarray data were normalized using frozen-RMA method[36] from the R package frma. Batch effect was corrected across series using ComBat[37], with histology as covariate.

Estimation of the TME composition

The TME composition of each tumour was assessed with the MCP-counter tool[9], which provides abundance scores for eight immune (T cells, $CD8^+$ T cells, cytotoxic lymphocytes, natural killer cells, B cell lineage, monocytic lineage, myeloid dendritic cells and neutrophils), and two stromal populations (endothelial cells and fibroblasts). The scores are based on analysis of transcriptomic markers—that is, transcriptomic features that are strongly, specifically and stably expressed in a unique cell population. These scores are proportional to the abundance of each cell population in the tumour, therefore allowing inter-sample comparison and large cohort analyses[38]. The MCP-counter signatures composition are as follows: T cells: *CD28*, *CD3D*, *CD3G*, *CD5*, *CD6*, *CHRM3-AS2*, *CTLA4*, *FLT3LG*, *ICOS*, *MAL*, *PBX4*, *SIRPG*, *THEMIS*, *TNFRSF25* and *TRAT1*; $CD8^+$ T cells: *CD8B*, cytotoxic lymphocytes: *CD8A*, *EOMES*, *FGFBP2*, *GNLY*, *KLRC3*, *KLRC4* and *KLRD1*; B lineage: *BANK1*, *CD19*, *CD22*, *CD79A*, *CR2*, *FCRL2*, *IGKC*, *MS4A1* and *PAX5*; natural killer cells: *CD160*, *KIR2DL1*, *KIR2DL3*, *KIR2DL4*, *KIR3DL1*, *KIR3DS1*, *NCR1*, *PTGDR* and *SH2D1B*; monocytic lineage: *ADAP2*, *CSF1R*, *FPR3*, *KYNU*, *PLA2G7*, *RASSF4* and *TFEC*; myeloid dendritic cells: *CD1A*, *CD1B*, *CD1E*, *CLEC10A*, *CLIC2* and *WFDC21P*; neutrophils: *CA4*, *CEACAM3*, *CXCR1*, *CXCR2*, *CYP4F3*, *FCGR3B*, *HAL*, *KCNJ15*, *MEGF9*, *SLC25A37*, *STEAP4*, *TECPR2*, *TLE3*, *TNFRSF10C* and *VNN3*; endothelial cells: *ACVRL1*, *APLN*, *BCL6B*, *BMP6*, *BMX*, *CDH5*, *CLEC14A*, *CXorf36* (also known as *DIPK2B*), *EDN1*, *ELTD1*, *EMCN*, *ESAM*, *ESM1*, *FAM124B*, *HECW2*, *HHIP*, *KDR*, *MMRN1*, *MMRN2*, *MYCT1*, *PALMD*, *PEAR1*, *PGF*, *PLXNA2*, *PTPRB*, *ROBO4*, *SDPR*, *SHANK3*, *SHE*, *TEK*, *TIE1*, *VEPH1* and *VWF*.

Intracohort immune classifications

The fibroblasts signature was removed from this analysis as all STS tumours exhibited high and homogeneous scores for this cell population, which is consistent with the mesenchymal origin of STS. The signature for CD8 T cells was removed from the analysis for GSE21050, GSE21122 and GSE30929 as it showed very small variation across all samples in these microarray-based cohorts. Unsupervised clustering of samples in each cohort was performed based on the metagene *Z*-score for the included populations of MCP-counter (Extended Data Fig. 9a–d) using R software, with the Euclidian distance and Ward's linkage criterion, using the gplots package. The TCGA SARC, GSE21050, GSE21122 and GSE30929 cohorts were separated into 6, 9, 7 and 6 groups, respectively. The number of clusters was chosen empirically following the dendrograms shown in Extended Data Fig. 9a–d. Analysis of the intersample variance revealed that much of the explainable variance was already attained at the chosen number of clusters as visualized in Extended Data Fig. 9e–h.

Pan-cohort immune classes

To aggregate the above four intracohort classifications, the transcriptome matrix of each cohort was independently zero-centred for each gene across all samples. Then, we computed the centroids of each class over the whole transcriptome and analysed the Pearson correlations between all the centroids on the set of genes shared across the four cohorts (Extended Data Fig. 9i). From these correlations, we deduced five SICs. The tumours from six remaining cohort-specific clusters shared intermediate/weak correlation patterns to other clusters and were temporarily labelled as 'unclassified'.

Prediction of the immune classes

Centroids of SICs were computed on MCP-counter intraseries *Z*-scores for T cells, cytotoxic lymphocytes, B cell lineage, natural killer cells, monocytic lineage, myeloid dendritic cells, neutrophils and endothelial cells, on all cohorts. To predict de novo the immune classes of each of the cohorts, MCP-counter *Z*-scores were computed, and each sample was assigned to the closest immune class based on its Euclidian distance to the related centroids. The SICs labels used are the ones predicted using this method. Principal component analysis of the 608 samples on the MCP-counter scores shows that the intra-SIC homogeneity was improved by this prediction step (Extended Data Fig. 9j, k), as confirmed by supervised tests across SICs (Extended Data Fig. 9l, m).

Gene signatures for the functional orientation

The signatures used to determine the functional orientation of the TME were derived from the literature[39]. The signatures were the following: immunosuppression (*CXCL12*, *TGFB1*, *TGFB3* and *LGALS1*), T cell activation (*CXCL9*, *CXCL10*, *CXCL16*, *IFNG* and *IL15*), T cell survival (*CD70* and *CD27*), regulatory T cells (*FOXP3* and *TNFRSF18*), major histocompatibility complex class I (*HLA-A*, *HLA-B*, *HLA-C*, *HLA-E*, *HLA-F*, *HLA-G* and *B2M*), myeloid cell chemotaxis (*CCL2*), and tertiary lymphoid structures (*CXCL13*). For each signature, scores were computed as the geometric mean signature expression.

De novo prediction of the immune classes of additional cohorts and other platforms

The predictor described above was adapted to analyse new and independent samples, from Nanostring-analysed FFPE samples. In a first step, SICs were estimated on the NTUH cohort by sorting samples on the B lineage signature, T cells signature then endothelial cell signature and assigning each sample according to the SIC it resembled the most. Similar to as described above, centroids of each SIC on Nanostring data MCP-counter scores *Z*-scores were computed and samples were reassigned to the SIC they were closest to the centroid of. For new samples from the SARC028 cohort, MCP-counter scores for T cells, cytotoxic lymphocytes, B lineage and endothelial cells were computed and transformed as *Z*-scores. Distances with Nanostring-defined centroids presented above were computed with Euclidian metric, and samples were assigned to the SIC with the lowest distance.

RNA extraction from FFPE tumours

Human FFPE tumour specimens were cut into 3-µm-thick sections and were reviewed under microscope for tumour histology. Non-tumour tissues were excluded and tumour tissues were deparaffinized by

deparaffinization solution (Qiagen 19093) and RNA were extracted by RNeasy FFPE kit (Qiagen 73504) according to the manufacturer's protocol. RNA quality and size distribution were determined by the Agilent 2100 Bioanalyzer with RNA analysis kits (RNA 6000 nano kit 5067-1511, RNA 6000 nano reagent 5067-1512, RNA 6000 nano ladder 5067-1529, RNA 6000 pico kit 5067-1513, RNA 6000 pico reagents 5067-1514, RNA 6000 pico ladder 5067-1535) for cohorts NTUH core and NTUH whole, and by the Agilent RNA ScreenTape assay (catalogue: RNA ScreenTape 5067-5576, RNA ScreenTape sample buffer 5067-5577, RNA ScreenTape ladder 5067-5578) and Agilent 2200 TapeStation for cohort SARC028. The samples from SAR028 were separately quality-controlled by the sarcoma pathology group at MD Anderson Cancer Center.

Nanostring nCounter analysis

The RNA was analysed using the nCounter Technology (Nanostring Technologies) as per the manufacturer's protocol. Data were normalized using the nSolver software (Nanostring Technologies).

Enzymatic and fluorescent multiplexed immunohistochemistry

The FFPE human tumour and control specimens were cut into 3-µm-thick sections. Human FFPE tonsil sections were used as positive controls for CD3, CD4, CD8, CD20, CD21, CD23, CD34, CXCR5, DC-LAMP, PD1, PDL1 and PNAd, placenta sections were used in addition for PDL1 and cerebral cortex tissue was used as a negative control. The specificity of all antibodies was tested by the manufacturers and the specificity of anti-PD1 antibodies was validated in our laboratory on overexpressing cells pellets as previously reported[40]. Antigen retrieval was carried out on a PT-link (Dako) using the EnVision FLEX Target Retrieval Solutions at High pH (Dako, K8004) or Low pH (Dako, K8005). Endogenous peroxidase activity and non-specific Fc receptor binding were blocked with H2O2 3% (Gifrer, 10603051) and Protein Block (Dako, X0909) respectively. The primary and secondary antibodies used for immunohistochemistry and immunofluorescence are summarized in Extended Data Table 2. Immunohistochemistry and immunofluorescence images were independently analysed blindly by three observers (L.L., C.S.-F. and G.L.).

Enzymatic immunohistochemistry

The stainings were performed with an Autostainer Link 48 (Dako). Chromogenic detection was performed using 3,3′-diaminobenzidine (Dako, K3468) for CD8, CD20, CD21, PDL1 and PNAd; 3-amino-9-ethylcarbazole substrate (Vector Laboratories, SK-4200) for DC-LAMP; Blue Alkaline Phosphatase Substrate (Vector Laboratories, SK5300) for CD3; HighDef red IHC chromogen (AP) (Enzo, ADI-950-140-0030) for CD20; and Permanent HRP Green (Zytomed Systems, ZUC070-100) for CD23 and CD34. The nuclei were counterstained with haematoxylin (Dako, S3301). After mounting with Glycergel Mounting Medium (Dako, C056330-2) or EcoMount (Biocare Medical, EM897L), the slides were scanned with a Nanozoomer (Hamamatsu). For CD3, CD8, CD20 and DC-LAMP markers, the density of positive cells per mm^2 was quantified with Calopix Software (Tribvn). For CD34 marker, the density of positive vessels per mm^2 was quantified with Halo10 software (Indica labs). TLS were identified using the registration module to fit one slide on the other (Halo10 software, Indica labs). Tumours were considered TLS-positive when a CD3 aggregate with DC-LAMP staining was found juxtaposing a CD20 aggregate. Only aggregates with surface above 60,000 $µm^2$, containing at least 700 cells and at least 350 $CD20^+$ cells were considered.

Fluorescent multiplexed immunohistochemistry

For the PD1, CD20 and CD3 3-plex staining, a tyramide system amplification (TSA) was used. The stainings were performed with a Leica Bond RX. The incubation with TSA reagent was performed after the incubation of the horseradish peroxidase (HRP)-conjugated polymer and was followed by antibody stripping at 97 °C for 10 min. This protocol was repeated for the second and third primary antibodies and corresponding polymer incubations. The dilutions used for the TSA are 1:400 for TSA AF488, 1:800 for TSA AF594 and 1:200 for TSA AF647, as per the manufacturer's recommendations. For the CXCR5, CD4 and PD1 3-plex staining, we used a conventional fluorescent-dye conjugated secondary antibody system performed manually (all secondary antibodies were diluted at 1:100). For all the fluorescent stainings, the nuclei were stained with DAPI Solution (Thermo Fisher, 62248) at 2 µg ml^{-1} for 10 min. After mounting with ProLongTM Gold Antifade Mountant (Thermofisher, P36934), the slides were scanned with a Zeiss Axio Scan.Z1.

Statistical analysis

All statistical analyses were performed using the R software (v.3.4.4) and the packages survival, gplots, dunn.test and FactoMineR. The relationship between two categorical variables was estimated with the chi-squared test. The relationship between a categorical variable and a quantitative variable was estimated with the Mann–Whitney *U* test (two categories) or the Kruskall–Wallis test (three or more categories). All tests were two-sided. In cases with three or more categories, pairwise comparisons were carried out with Dunn tests. The relationship between two quantitative variables was estimated with the Pearson correlation. When appropriate, *P* values were corrected for multiple hypothesis testing with the Bonferroni or Benjamini–Hochberg methods, as specified in the text or figure legends. Survival was analysed with Kaplan–Meier estimates and log-rank tests. No statistical methods were used to predetermine sample size. The experiments were not randomized, and investigators were not blinded to allocation during experiments and outcome assessment unless stated otherwise.

Reporting summary

Further information on research design is available in the Nature Research Reporting Summary linked to this paper.

Data availability

The transcriptomic datasets analysed in this study can be accessed on the GDC Portal (portal.gdc.cancer.gov, cohort TCGA SARC) and the GEO repository under accession numbers GSE21050, GSE21122 and GSE30929. FSG cohort data are publicly available from ArrayExpress for gastrointestinal stromal tumour with accession code E-MTAB-373, and from the GEO for synovial sarcomas with accession number GSE40021. Myxoid liposarcomas from the FSG cohort are available from the corresponding authors upon reasonable request. Immunohistochemistry and gene expression data related to the NTUH cohort (Fig. 3, Extended Data Figs. 7, 8) are available upon reasonable request to W.H.F. (herve.fridman@crc.jussieu.fr). The data that support the findings related to Fig. 4 are available from SARC but restrictions apply to the availability of these data, which were used under license for the study. Data are, however, available from H.A.T. (htawbi@mdanderson.org) upon reasonable request and with permission of SARC.

Code availability

All code used in this study is available from the corresponding author upon reasonable request.

31. Chibon, F. et al. Validated prediction of clinical outcome in sarcomas and multiple types of cancer on the basis of a gene expression signature related to genome complexity. *Nat. Med.* **16**, 781–787 (2010).
32. Barretina, J. et al. Subtype-specific genomic alterations define new targets for soft-tissue sarcoma therapy. *Nat. Genet.* **42**, 715–721 (2010).
33. Gobble, R. M. et al. Expression profiling of liposarcoma yields a multigene predictor of patient outcome and identifies genes that contribute to liposarcomagenesis. *Cancer Res.* **71**, 2697–2705 (2011).
34. Lagarde, P. et al. Mitotic checkpoints and chromosome instability are strong predictors of clinical outcome in gastrointestinal stromal tumors. *Clin. Cancer Res.* **18**, 826–838 (2012).
35. Lagarde, P. et al. Chromosome instability accounts for reverse metastatic outcomes of pediatric and adult synovial sarcomas. *J. Clin. Oncol.* **31**, 608–615 (2013).
36. McCall, M. N., Bolstad, B. M. & Irizarry, R. A. Frozen robust multiarray analysis (fRMA). *Biostatistics* **11**, 242–253 (2010).

37. Johnson, W. E., Li, C. & Rabinovic, A. Adjusting batch effects in microarray expression data using empirical Bayes methods. *Biostatistics* **8**, 118–127 (2007).
38. Petitprez, F. et al. Transcriptomic analysis of the tumor microenvironment to guide prognosis and immunotherapies. *Cancer Immunol. Immunother.* **67**, 981–988 (2017).
39. Beuselinck, B. et al. Molecular subtypes of clear cell renal cell carcinoma are associated with sunitinib response in the metastatic setting. *Clin. Cancer Res.* **21**, 1329–1339 (2015).
40. Giraldo, N. A. et al. Orchestration and prognostic significance of immune checkpoints in the microenvironment of primary and metastatic renal cell cancer. *Clin. Cancer Res.* **21**, 3031–3040 (2015).

Acknowledgements This work was supported by the Institut National de la Santé et de la Recherche Médicale, the Université de Paris, Sorbonne University, the Programme Cartes d'Identité des Tumeurs (CIT) from the Ligue Nationale Contre le Cancer, grants from Institut National du Cancer (HTE-INSERM plan cancer, C16082DS), Association pour la Recherche sur le Cancer (ARC), Cancer Research for Personalized Medecine programme (CARPEM T8), French Sarcoma Group, the European Connective Tissue Cancer Network (CONTICANET, FP6-018806), 'FONCER contre le cancer' programme, Labex Immuno-Oncology (LAXE62_9UMRS972 FRIDMAN), the National Institutes of Health (E.Z.K. is supported by T32CA0095999) and the Moon Shot program at MD Anderson Cancer Center. Grants from the Ministry of Education (NTU-107L9014) and Ministry of Science and Technology (MOST 107-3017-F-002 -002-), Taiwan and from the National Taiwan University (YongLin Chair Grant S-01 and S-03) also supported this study. SARC028 was jointly funded by Merck, Inc., SARC, Sarcoma Foundation of America, and the QuadW Foundation. F.P. supported by CARPEM doctorate fellowship. C.L.R. is recipient of the Paul Calabresi Clinical Oncology Award (K12 CA088084). The slides stained for immunofluorescence were scanned and analysed at the Centre d'Histologie, d'Imagerie et de Cytométrie (CHIC), Centre de Recherche des Cordeliers UMRS1138 (Paris, France). CHIC is a member of the Sorbonne University Flow Cytometry Network (RECYF). We thank C. Klein, K. Garbin and E. Devevre for their support with the imaging. The Nanostring analysis of the NTUH core cohort was performed by the Plateforme Génomique of the Institut Curie (Paris, France). We thank D. Gentien and E. Henry for their support. We acknowledge the help of H. Yan and B. Singh.

Author contributions F.P., W.H.F., C.S.-F., A.d.R., T.W.-W.C., H.A.T. and A.I. designed the study and experiments. F.P., A.d.R., C.L. and Y.L. performed the bioinformatics analysis. L.L., G.L., I.N., L.-P.H., A.B., M.M. and F.P. carried out the immunohistochemistry experiments. J.C., Y.-M.J. and J.A. performed anatomo-pathology revision on the samples. E.Z.K., C.-M.S., W.-L.W. and K.M.W. performed the RNA extraction and Nanostring experiments. T.W.-W.C., A.I., M.T. and H.A.T. provided clinical guidance. T.W.-W.C., M.T., A.I., E.Z.K., A.J.L., C.L.R., M.A.B., V.B., D.R. and H.A.T. cared for the patients and provided patient materials or clinical data. F.P., W.H.F., C.S.-F., H.A.T., A.d.R., E.Z.K., C.L.R., A.J.L., T.W.-W.C., C.-M.S., J.A.W. and A.I. discussed the data and wrote the text. W.H.F., C.S.-F., A.d.R. and H.A.T. supervised the study and all authors commented on the manuscript and approved the submission.

Competing interests W.H.F. is a consultant for AstraZeneca, Novartis, Servier and Pierre Fabre. A.I. serves in the advisory board of Bayer, Daiichy, Epizyme, Lilly, Novartis, Roche and Springworks, and received research funding from Astra Zeneca, Bayer, Chugai, Merck, MSD, Novartis and Pharmamar. J.A. is a consultant for AstraZeneca, Bayer, BMS, MSD and Roche and received research funding from MSD, Pfizer and Pierre Fabre. J.A.W. participated on advisory boards for Merck, BMS, Novartis, Astra Zeneca, Roche Genentech and Illumina. M.A.B. is a consultant for EMD Serono, Immune Design, Eisai. H.A.T. serves on advisory boards and receives consulting fees from BMS, Merck and Genentech, and received research funding from BMS, Merck, Celgene, GSK, and Genentech. T.W.-W.C. participated in advisory boards for Eisai and Lilly and received research funds from Eisai. C.L.R. received research funding from BMS. The other authors declare no conflict of interest.

Additional information

Supplementary information is available for this paper at https://doi.org/10.1038/s41586-019-1906-8.

Correspondence and requests for materials should be addressed to H.A.T. or W.H.F.

Peer review information *Nature* thanks Naiyer Rizvi and the other, anonymous, reviewer(s) for their contribution to the peer review of this work.

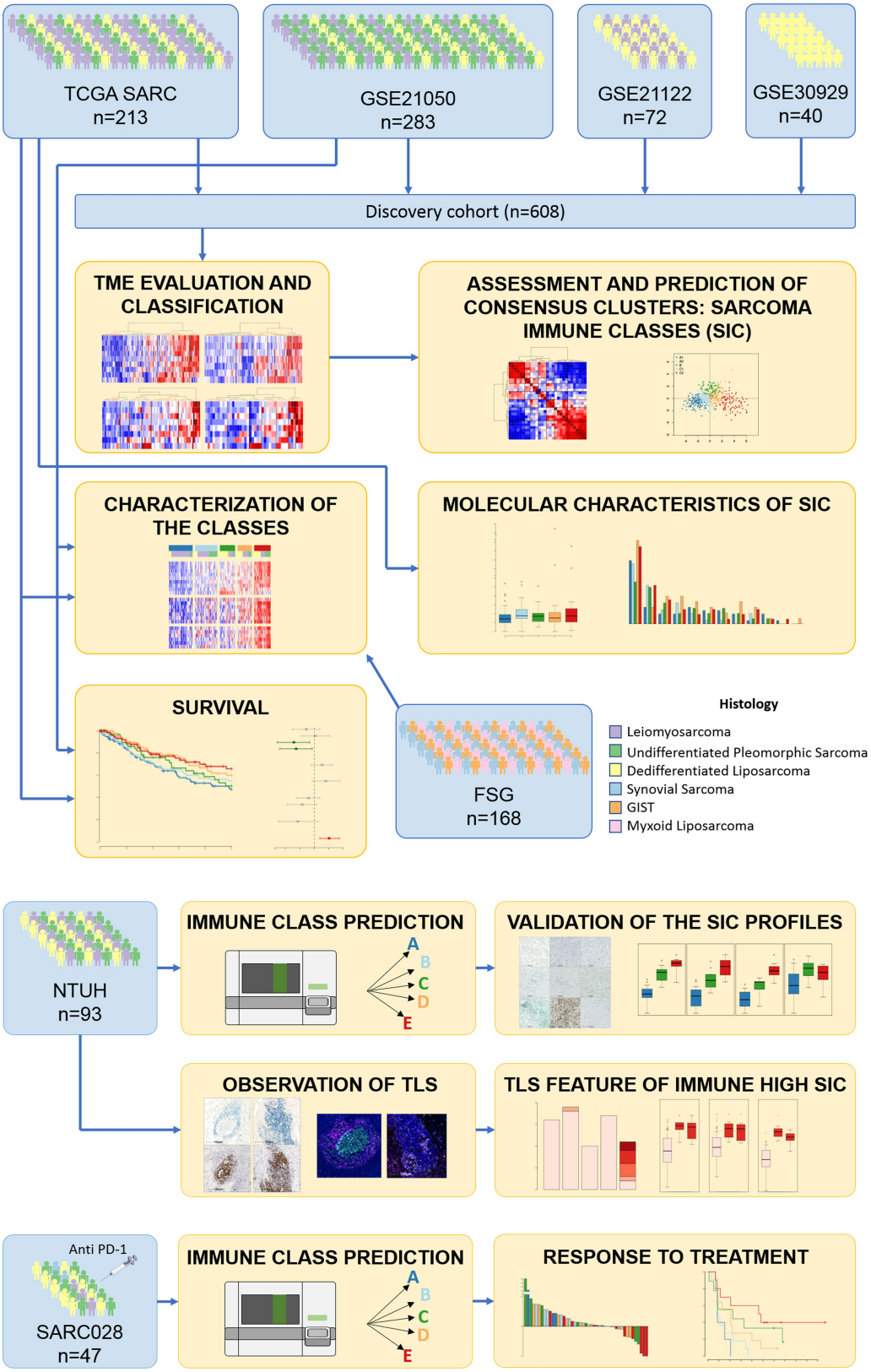

Extended Data Fig. 1 | Diagram of analytic workflow. The drawing of the syringe in the bottom left corner originates from Servier Medical Art (https://smart.servier.com), and is distributed under a CC-BY 3.0 Attribution license (https://creativecommons.org/licenses/by/3.0/).

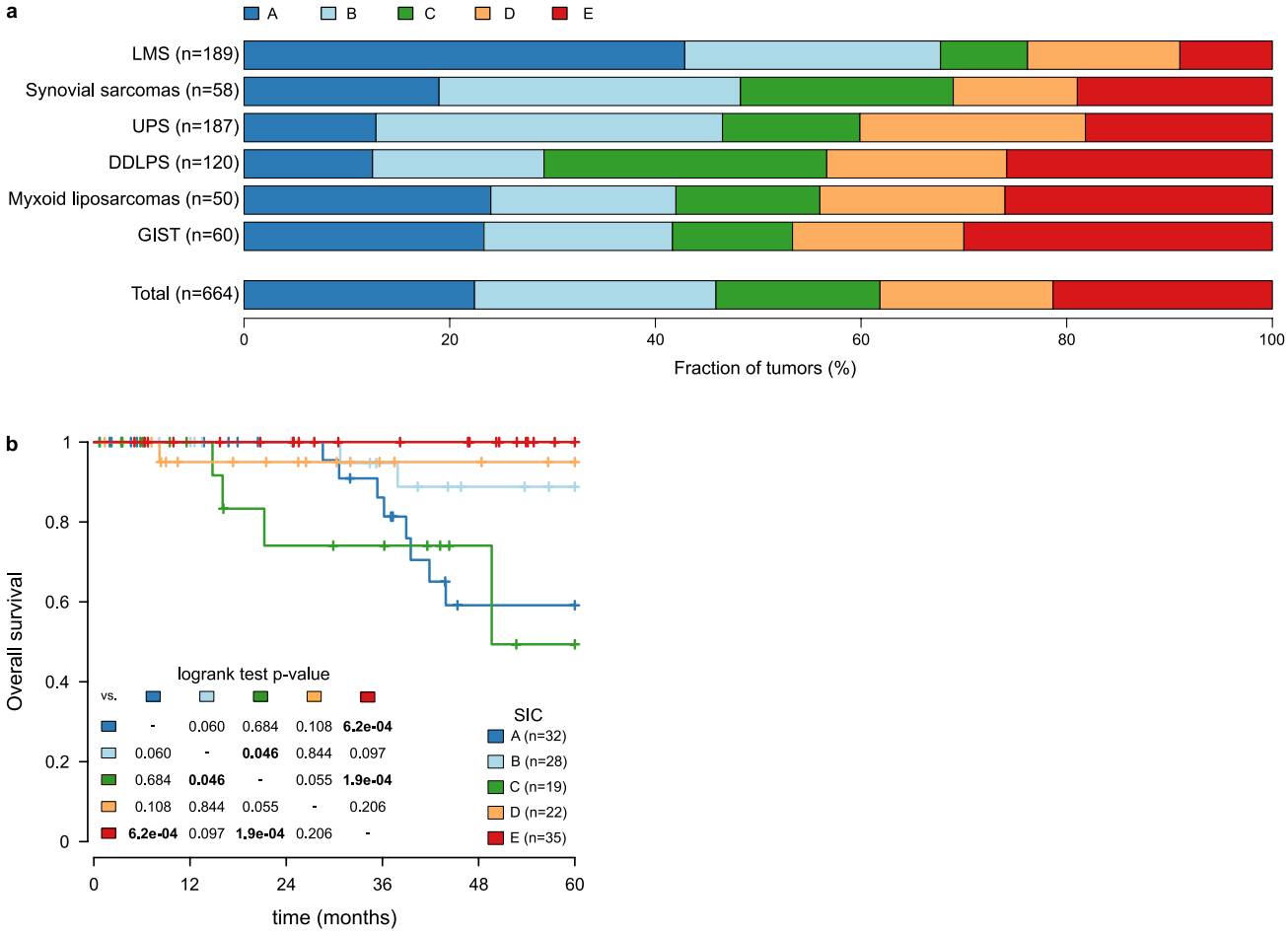

Extended Data Fig. 2 | SICs in various STS histologies. a, Repartition of the SICs in various histologies of TCGA SARC and GSE21050 (LMS, UPS and DDLPS), and FSG cohort (synovial sarcoma, myxoid liposarcoma, gastrointestinal stromal tumour (GIST)). **b**, Survival of patients from the FSG cohort ($n = 136$) according to SIC classification. Patients with synovial sarcoma, myxoid liposarcoma and gastrointestinal stromal tumour were pooled. Analysis was performed with Kaplan–Meier estimates and two-sided log-rank tests.

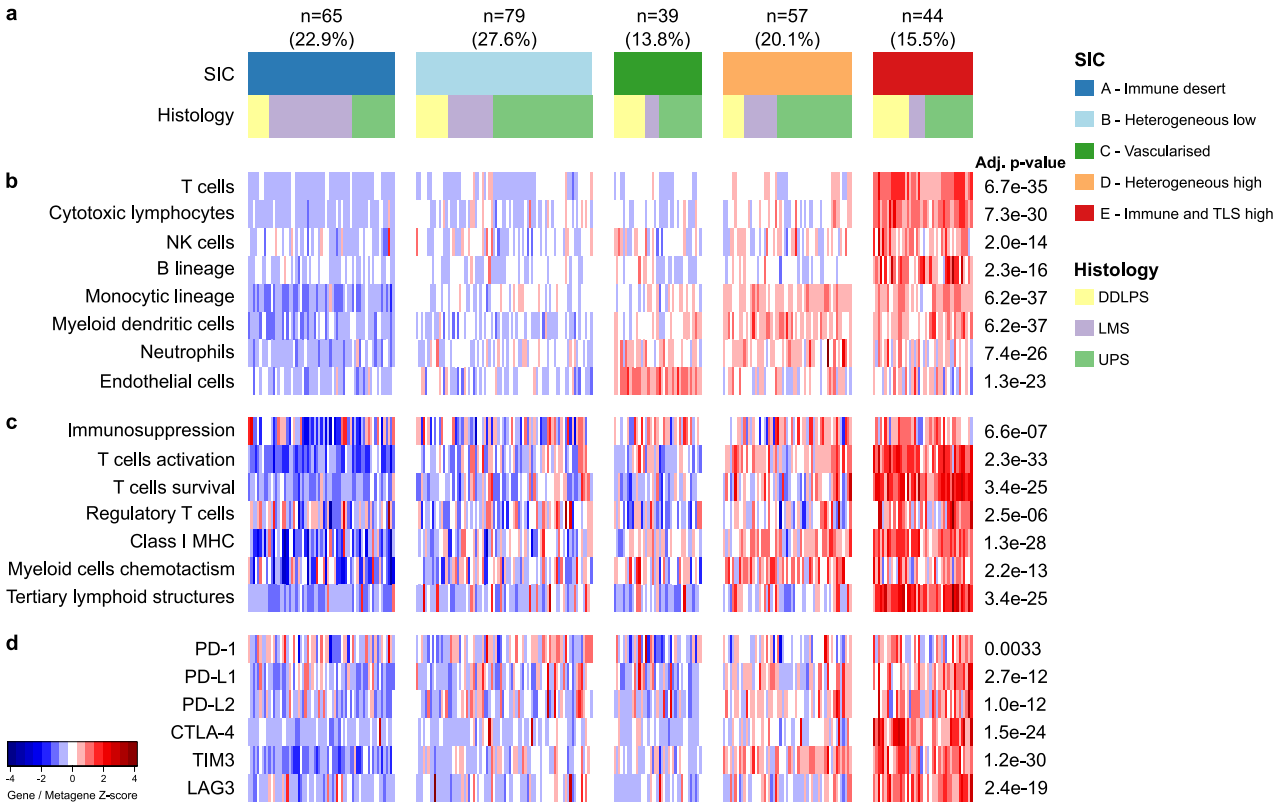

Extended Data Fig. 3 | The SICs exhibit strongly different TMEs. This figure refers to the GSE21050 cohort ($n = 283$). **a**, Composition of the GSE21050 cohort by SIC, histology and site of disease. **b**, Composition of the TME by SIC as defined by the MCP-counter *Z*-scores. **c**, Expression of gene signatures related to the functional orientation of the immune TME by SIC. **d**, Expression of genes related to immune checkpoints by SIC. Adjusted *P* values are obtained from Benjamini–Hochberg correction of two-sided Kruskal–Wallis test *P* values. These observations stand for cohorts GSE21122 and GSE30929 (not shown).

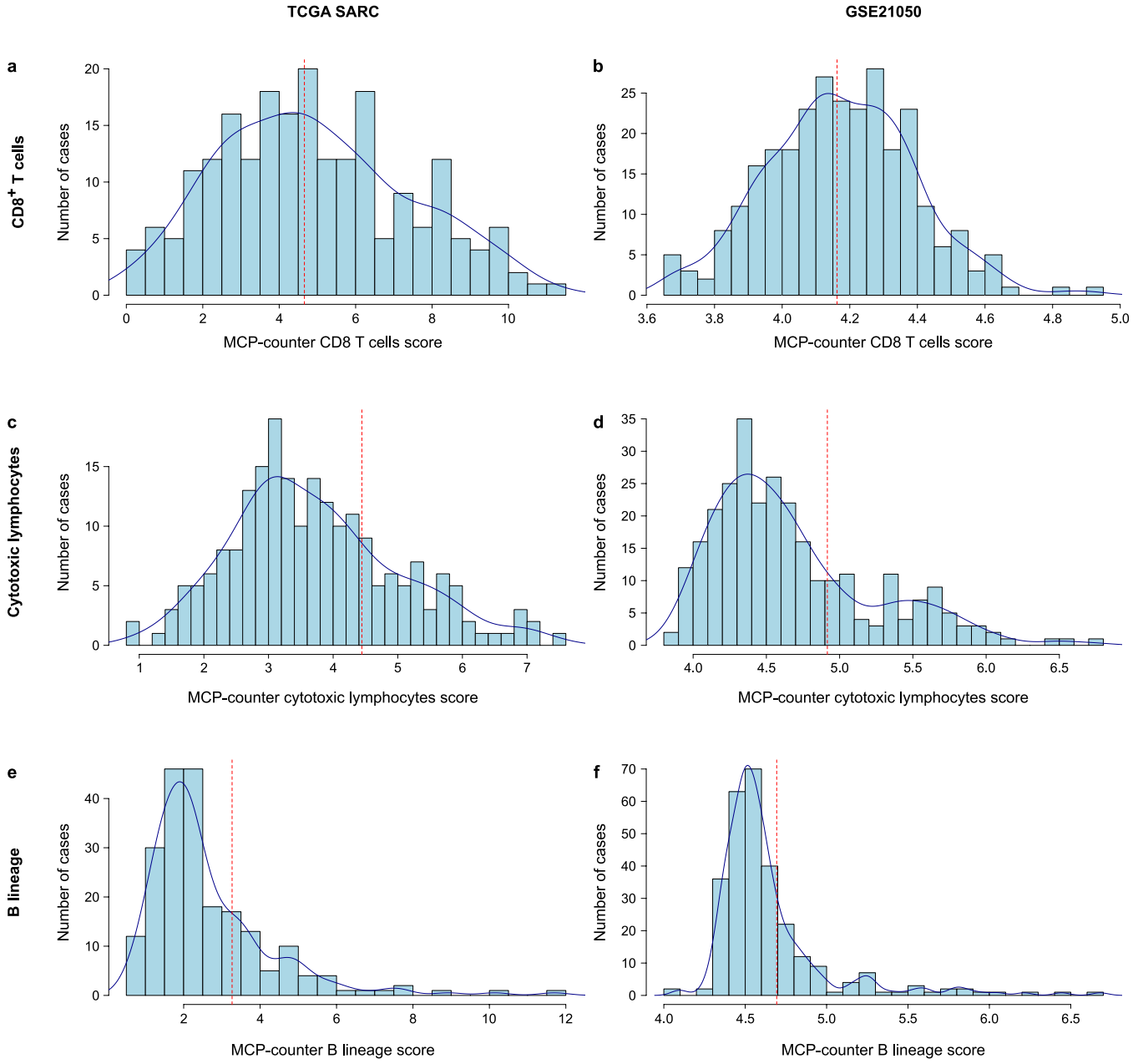

Extended Data Fig. 4 | Distribution of MCP-counter scores. a–**e**, MCP-counter scores in TCGA SARC ($n = 213$) (**a**, **c**, **e**) and GSE21050 ($n = 283$) (**b**, **d**, **e**), for $CD8^+$ T cells (**a**, **b**), cytotoxic lymphocytes (**c**, **d**) and B lineage cells (**e**, **f**). The blue line indicates the density curve. The red dotted line indicates the cut-off chosen to segregate high or low values, set at the median for $CD8^+$ T cells and at the third quartile for cytotoxic lymphocytes and B lineage, in each cohort. These values were chosen because the CD8 T cells scores present a normal distribution, whereas the cytotoxic lymphocytes and B lineage scores distribution exhibit a long right tail.

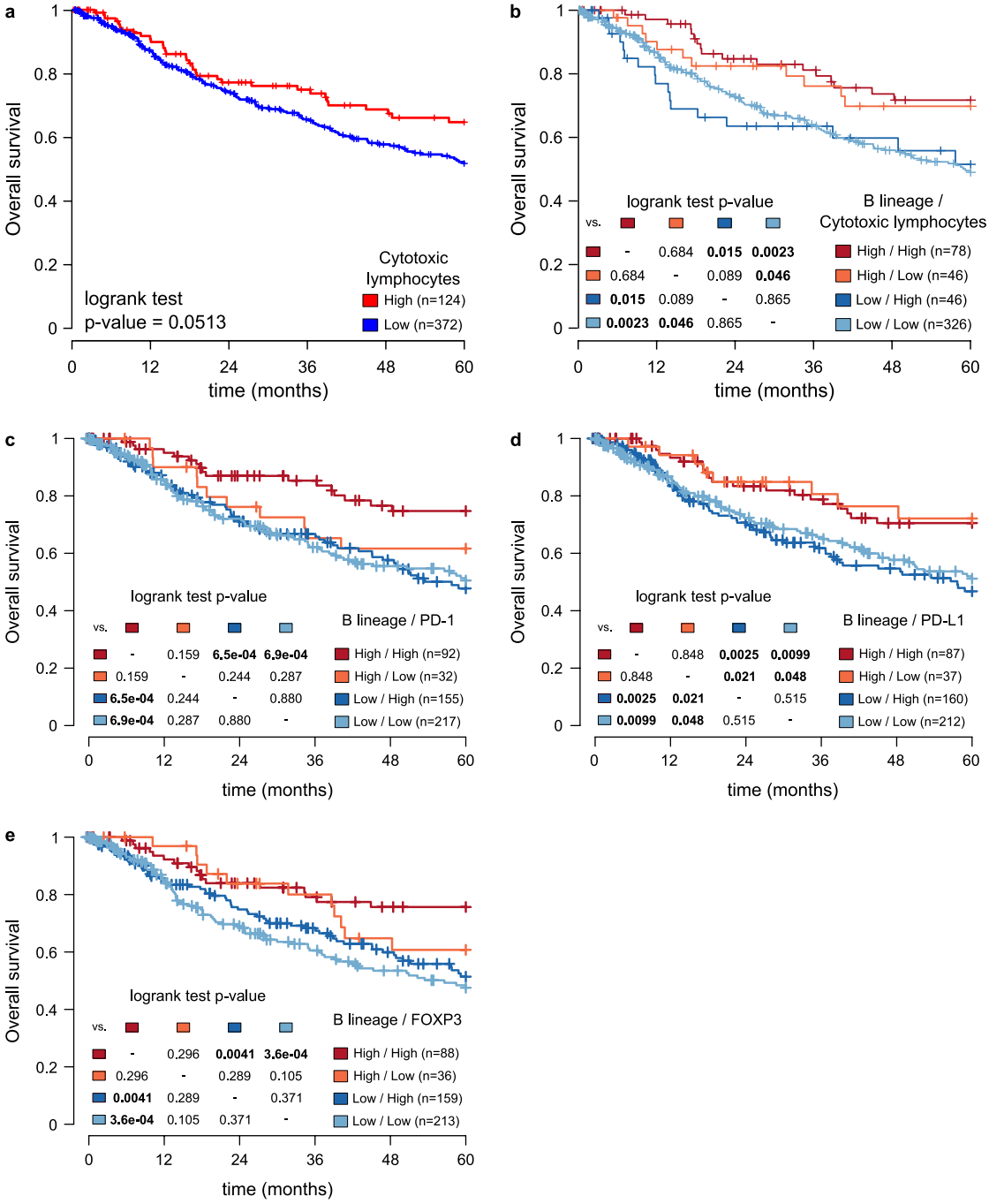

Extended Data Fig. 5 | B cell infiltration of STS is the key factor associated with overall survival. This figure refers to TCGA SARC and GSE21050 pooled cohorts ($n = 496$). **a**, Overall survival of patients with STS according to MCP-counter scores for cytotoxic lymphocytes. **b**, Overall survival of patients based on the infiltration level of their tumours by B lineage cells and cytotoxic lymphocytes. **c**–**e**, Overall survival of patients based on degree of tumour infiltration by B lineage cells and expression of *PDCD1* (**c**), *CD274* (**d**) and *FOXP3* (**e**). The analyses were performed with the Kaplan–Meier estimates and two-sided log-rank tests. Tumours were considered high for expression of *PDCD1*, *CD274* and *FOXP3* if their expression was above median, and high for B lineage and cytotoxic lymphocytes if the MCP-counter score was above the third quartile.

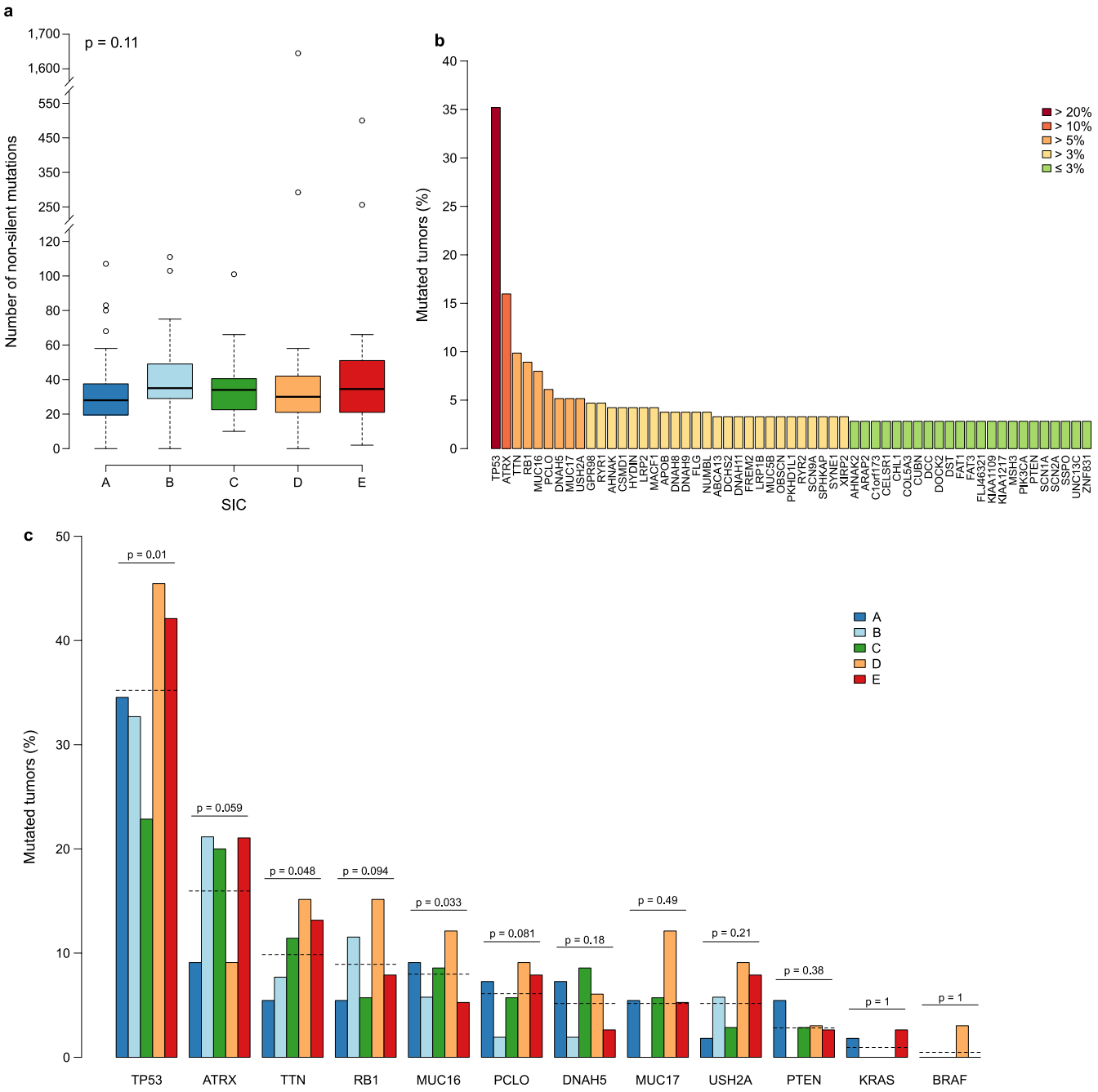

Extended Data Fig. 6 | The mutational landscape of STS tumours does not vary significantly between SICs. This figure refers to the TCGA SARC cohort ($n = 213$). **a**, Mutational burden according to the SIC of the tumours, expressed in number of non-silent mutations. *P* value was computed with a Kruskal–Wallis test. Box plots as in Fig. 3d. **b**, Mutation frequency of all genes that are mutated in greater than 2.5% of tumours. **c**, Mutation frequency for genes that are mutated in more than 5% of tumours, according to SICs in the TCGA SARC cohort. The dashed lines indicate the overall mutation frequency. *P* values were obtained through one-sample two-sided *t*-tests, corrected for multiple testing with the Bonferroni method. This was applied only to samples that had mutations on the considered genes (*TP53*: $n = 75$; *ATRX*: $n = 34$; *TTN*: $n = 21$; *RB1*: $n = 19$; *MUC16*, $n = 17$; *PCLO*, $n = 13$; *DNAH5*, *MUC17* and *USH2A*: $n = 11$, *PTEN*, $n = 6$; *KRAS*, $n = 2$; *BRAF*, $n = 1$).

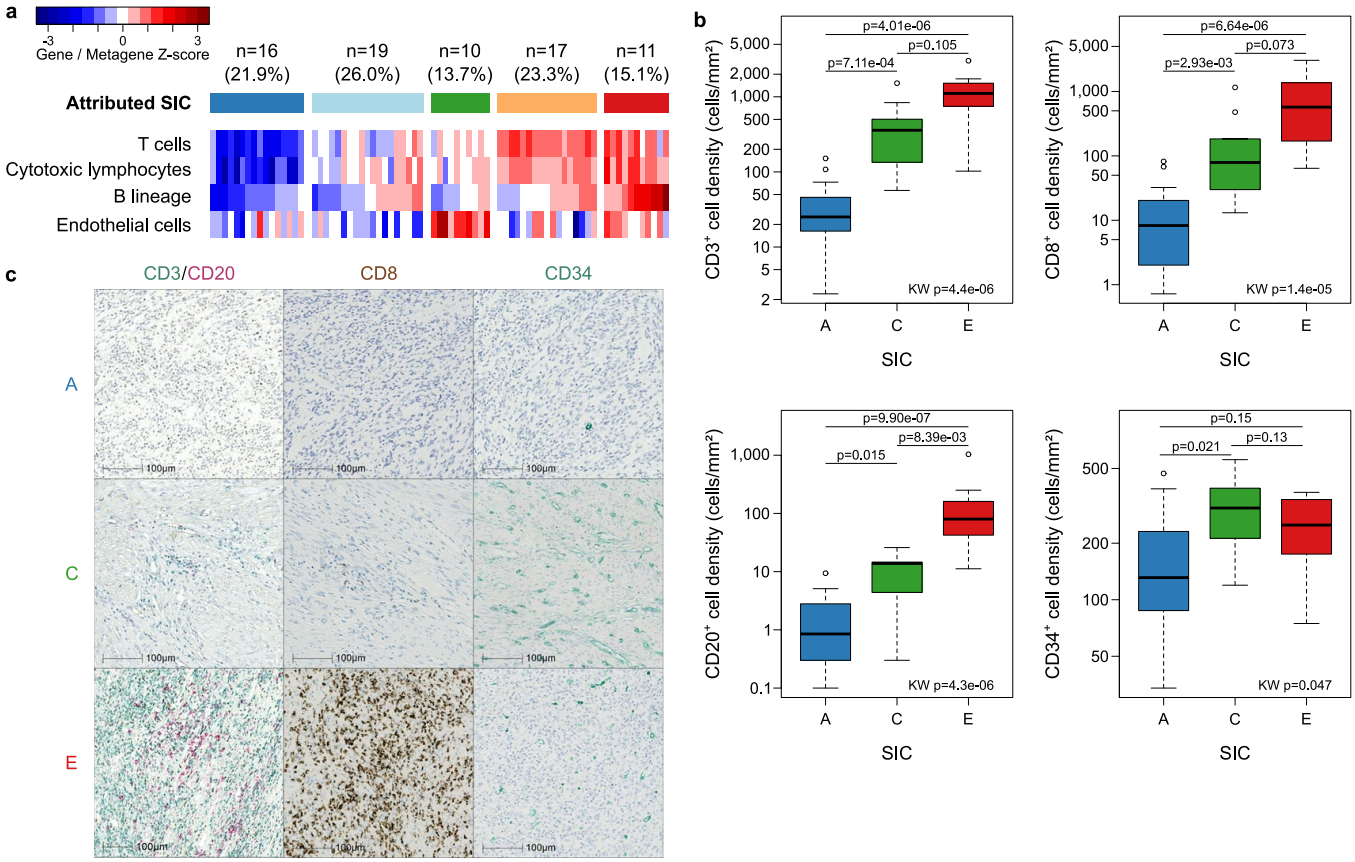

Extended Data Fig. 7 | Validation of SIC profiles by immunohistochemistry. This figure refers to the NTUH cohort. **a**, SIC attribution as defined by gene expression using the MCP-counter *Z*-scores in 73 cases. **b**, Cell density counts showing the differences in TME composition according to SIC identification of the 73 cases (SIC A: $n=16$; SIC C: $n=10$; SIC E: $n=11$). *P* values are determined by two-sided Kruskal–Wallis (KW) tests. Pairwise comparisons are derived from the Dunn test. Box plots are as in Fig. 3d. **c**, Representative images of CD3 (green), CD20 (pink), CD8 (brown) and CD34 (green) expression by immunohistochemistry of SIC A, C and E tumours. The same area of the tumour is represented (0.05 mm^2) in each image. Similar results were observed on the other tumours from the same SICs (SIC A: $n=16$; SIC C: $n=10$; SIC E: $n=11$).

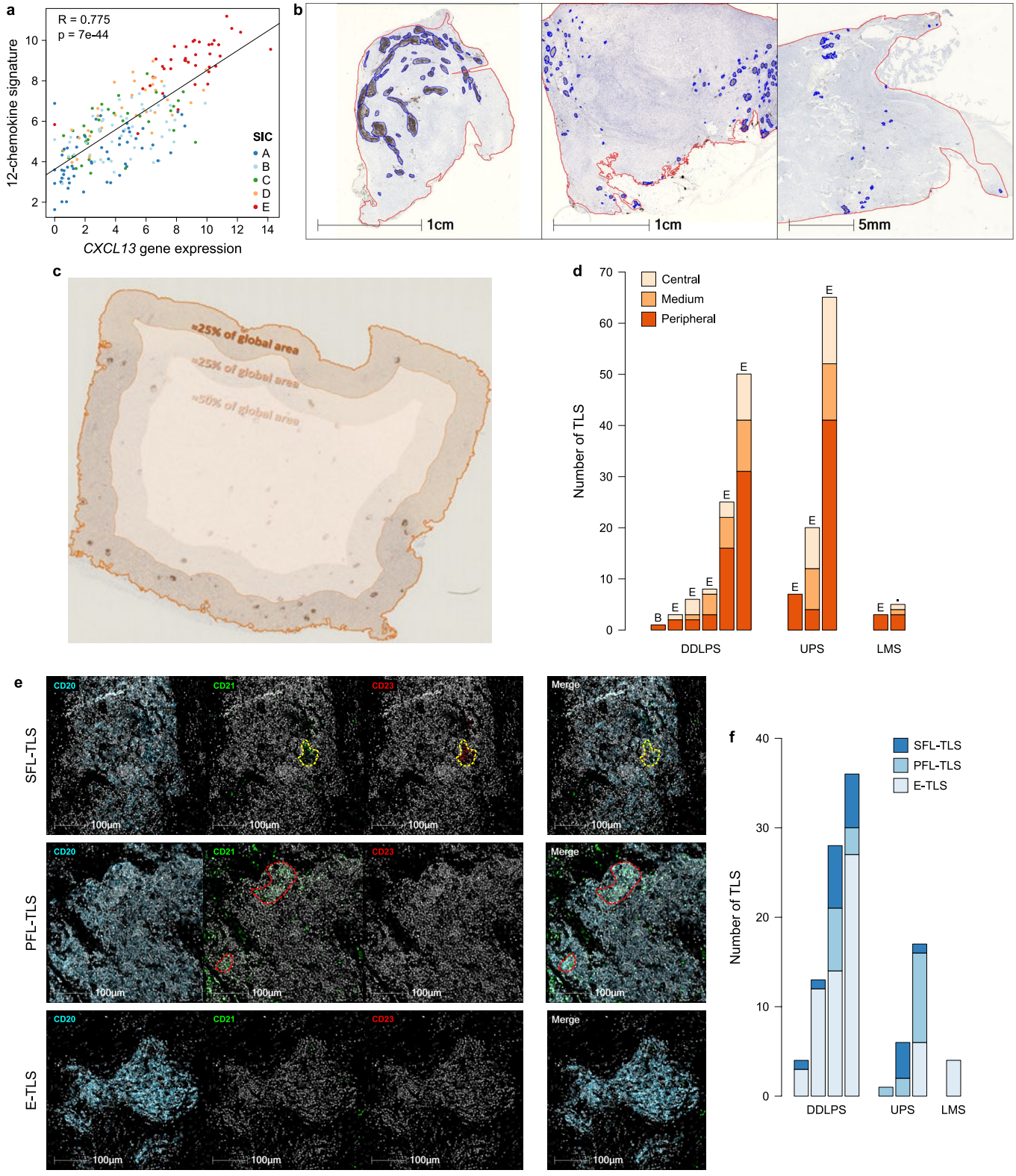

Extended Data Fig. 8 | See next page for caption.

Extended Data Fig. 8 | Location and maturation of TLSs. a, Pearson correlation between the expression of CXCL13 and the 12-chemokine signature of TLS in TCGA SARC cohort ($n = 213$). Samples are coloured according to SICs. **b**, Intratumoural location of TLSs in three different examples from the NTUH cohort—DDLPS, UPS and LMS, respectively. TLSs are observed by the presence of $CD20^+$ B cells aggregates (brown, surrounded by blue shapes). The red line delineates the tumoral zone. Similar findings were observed on the 11 tumours with TLS. **c**, Definition of peripheral, medium and central zones, accounting for 25%, 25% and 50% of the total tumour area, respectively. **d**, Distribution of TLSs in the various zones. Each bar represents one tumour. The letters above bars indicate the SIC of the tumour when the sample passed quality control of Nanostring nCounter hybridization. Dots indicate tumours in which SIC could not be determined because of RNA quality control. Similar images were observed for 66 E-TLS, 23 PFL-TLS and 20 SFL-TLS. **e**, Illustration of diverse degrees of TLS maturation in STS tumours. Consistent with maturation events occurring in secondary lymphoid organs, three maturation steps have been described for TLS: E-TLS (bottom), PFL-TLS (middle) and SFL-TLS (top), which differ in the presence of follicular dendritic cells (FDC) and their markers. E-TLS contain aggregates of $CD20^+$ B cells and $CD3^+$ T cells without FDC, PFL-TLS contain $CD21^+$ FDC (red dotted zones) and SFL-TLS contain a germinal centre, notably visible through the presence of $CD21^+CD23^+$ follicular dendritic cells (yellow dotted zone). DAPI staining is shown in white. DAPI-negative green dots correspond to fluorescent erythrocytes. **f**, Distribution of TLS maturation steps in a subset of tumours. Each bar represents one tumour. Differences between the number of TLSs observed here and in other figures can be explained by use of non-consecutive slides or a different tumour block for some samples.

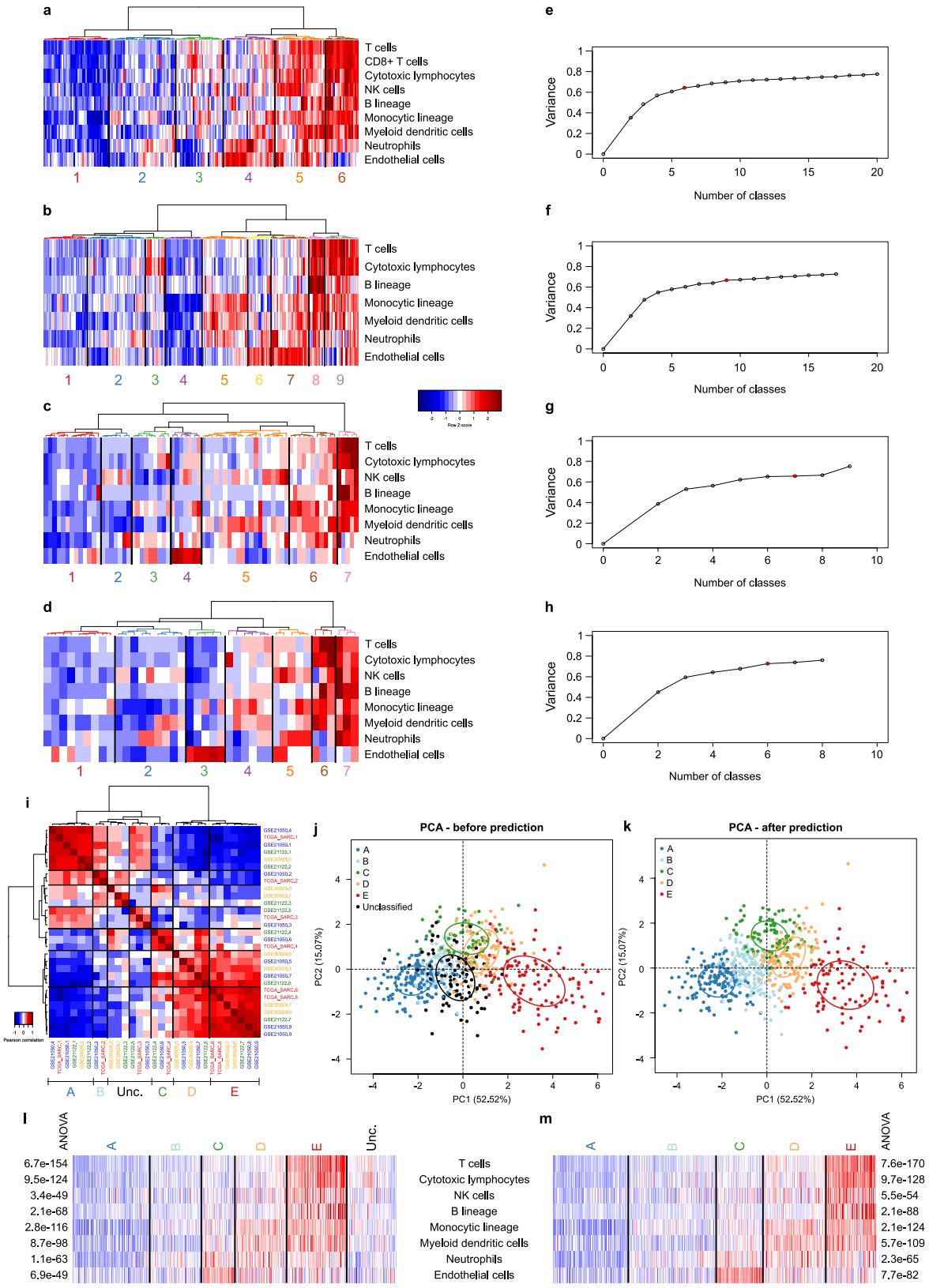

Extended Data Fig. 9 | See next page for caption.

Extended Data Fig. 9 | Pan-cohort immune classification. This figure refers to the four discovery cohorts: TCGA SARC ($n = 213$), GSE21050 ($n = 283$), GSE21122 ($n = 72$) and GSE30929 ($n = 40$). **a**–**d**, Heat map and unsupervised hierarchical clustering of the MCP-counter scores describing the tumour microenvironment. Each of the population is represented by the *Z*-scores of the signature. **a**, TCGA SARC. **b**, GSE21050. **c**, GSE21122. **d**, GSE30929. **e**–**h**, Evolution of the variance explained by the clusters as a function of the number of clusters. Red dots indicate the number of clusters that was retained in this study. Each graph corresponds to the heat map on its left. **i**, Heat map of the Pearson correlation of centroids from each SIC class of discovery cohorts (TCGA SARC, GSE21050, GSE21122 and GSE30929, $n = 608$), with five immune classes and two groups of unclassified samples. **j**, **k**, Principal component analysis of samples from the four discovery cohorts ($n = 608$), based on their normalized and merged MCP-counter scores. **j** is coloured according to the original classes, **k** is coloured according to the predicted immune classes, showing a heightened homogeneity within each SIC class. **l**, **m**, Composition of the TME with classes defined as in **j** and **k** for the four discovery cohorts ($n = 608$), expressed in cohort-specific row *Z*-scores.

Extended Data Table 1 | Clinicopathological composition of the cohorts included in this study

Cohort	TCGA SARC	GSE21050	GSE21122	GSE30929	FSG	NTUH	SARC028
n	213	283	72	40	168	93 (SIC: 73)	47
Age (median, range)	63 (33-90)	63 (15-92)	ND	ND	36 (1-83)	58 (9-94)	57 (25-83)
Gender (n, %)							
Male	98 (46%)	131 (48.7%)	ND	ND	99 (58.9%)	37 (39.8%)	34 (72.3%)
Female	114 (54%)	138 (51.3%)	ND	ND	69 (41.1%)	56 (60.2%)	13 (27.7%)
STS histology (n,%)							
DDLPS	58 (27.2%)	62 (21.9%)	46 (63.9%)	40 (100%)	0 (0%)	30 (32.3%)	19 (40.4%)
LMS	104 (48.8%)	85 (30%)	26 (36.1%)	0 (0%)	0 (0%)	31 (33.3 %)	6 (12.8%)
UPS	51 (23.9%)	136 (48.1%)	0 (0%)	0 (0%)	0 (0%)	32 (34.4%)	19 (40.4%)
Synovial sarcoma	0 (0%)	0 (0%)	0 (0%)	0 (0%)	58 (34.5%)	0 (0%)	3 (6.4%)
Myxoid liposarcoma	0 (0%)	0 (0%)	0 (0%)	0 (0%)	50 (29.8%)	0 (0%)	0 (0%)
GIST	0 (0%)	0 (0%)	0 (0%)	0 (0%)	60 (35.7%)	0 (0%)	0 (0%)
SIC (n,%)							
A	55 (25.8%)	65 (23%)	14 (19.4%)	8 (20%)	37 (22%)	16 (21.9%)	5 (10.6%)
B	52 (24.4%)	78 (27.6%)	22 (30.6%)	13 (32.5%)	37 (22%)	19 (26%)	11 (23.4%)
C	35 (16.4%)	39 (13.9%)	8 (11.1%)	6 (15%)	26 (15.5%)	10 (13.7%)	9 (19.1%)
D	33 (15.5%)	57 (20.1%)	21 (29.2%)	7 (17.5%)	26 (15.5%)	17 (23.3%)	12 (25.5%)
E	38 (17.8%)	44 (15.5%)	7 (9.7%)	6 (15%)	42 (25%)	11 (15.1%)	10 (21.3%)

For cohort GSE21050, sex information could not be retrieved for 14 patients. For cohort NTUH, SIC could be determined for 73 patients only. NA, not available.

Extended Data Table 2 | Antibodies used for immunohistochemistry and immunofluorescence

Antibody	References	Species	Clone	Source	Concentration (ug/mL)	Antigen Retrieval	Secondary Antibody	Tertiary Reagents
Immunohistochemistry								
CD3	790-4341	Rabbit	2GV6	Roche	0.4	pH9	Alkaline Phosphatase Goat Anti-Rabbit IgG	Alkaline Phosphatase Blue Substrate
CD8	M7103	Mouse IgG1	C8/144B	Agilent	1.57	pH9	EnVision+ System-HRP, Labelled Polymer (Mouse)	DAB
CD20	M0755	Mouse IgG2a	L26	Agilent	0.6	pH6	EnVision+ System-HRP, Labelled Polymer (Mouse)	DAB
							Polyview Plus AP (anti-mouse) reagent	HighDef red IHC chromogen (AP)
CD21	M0784	Mouse IgG1	1F8	Agilent	6.6	pH6	EnVision+ System-HRP, Labelled Polymer (Mouse)	DAB
CD23	ab16702	Rabbit	SP23	Abcam	0.5	pH9	EnVision+ System-HRP, Labelled Polymer (Rabbit)	Permanent HRP Green
CD34	M7165	Mouse IgG1	Qbend-10	Agilent	0.48	pH6	EnVision+ System-HRP, Labelled Polymer (Mouse)	Permanent HRP Green
DC-Lamp	DDX0191	Rat IgG2a	1010E1.01	Dendritics	5	pH9	Biotin Donkey Anti-Rat IgG	AEC Peroxidase (HRP) Substrate
PD-L1	13684	Rabbit	E1L3N	Cell Signaling	1.25	pH9	EnVision+ System-HRP, Labelled Polymer (Rabbit)	DAB
PNAd	553863	Rat IgM	MECA-79	BD	5	pH6	ImmPRESS HRP Anti-Rat (Peroxidase) Polymer Detection Kit	DAB
Immunofluorescence								
CD3	790-4341	Rabbit	2GV6	Roche	0.4	pH9	EnVision+ System-HRP, Labelled Polymer (Rabbit)	Alexa Fluor™ 647 Tyramide Reagent
CD4	AC-0173	Rabbit	EP204	Epitomics	0.17	pH9	Cy3 Donkey Anti-Rabbit IgG	NA
CD20	M0755	Mouse IgG2a	L26	Agilent	0.6	pH6	EnVision+ System-HRP, Labelled Polymer (Mouse)	Alexa Fluor™ 594 Tyramide Reagent
					1.2	pH 6	Cy5 Goat Anti-Mouse IgG2a	NA
CD21	M0784	Mouse IgG1	1F8	Agilent	7.5	pH 6	Cy3 Goat Anti-Mouse IgG1	NA
CD23	ab16702	Rabbit	SP23	Abcam	2	pH 6	FITC Donkey Anti-Rabbit IgG	NA
CXCR5	MAB190-100	Mouse IgG2b	51505	R&D	5	pH9	FITC Rat Anti-Mouse IgG2b	NA
PD-1	NA	Mouse IgG2a	EH33	CoStim	3	pH6	EnVision+ System-HRP, Labelled Polymer (Mouse)	Alexa Fluor™ 488 Tyramide Reagent
					6	pH9	Cy5 Goat Anti-Mouse IgG2a	NA

nature research

Corresponding author(s): Wolf H Fridman

Last updated by author(s): Nov 4, 2019

Reporting Summary

Nature Research wishes to improve the reproducibility of the work that we publish. This form provides structure for consistency and transparency in reporting. For further information on Nature Research policies, see Authors & Referees and the Editorial Policy Checklist.

Statistics

For all statistical analyses, confirm that the following items are present in the figure legend, table legend, main text, or Methods section.

n/a	Confirmed
☐	☒ The exact sample size (*n*) for each experimental group/condition, given as a discrete number and unit of measurement
☐	☒ A statement on whether measurements were taken from distinct samples or whether the same sample was measured repeatedly
☐	☒ The statistical test(s) used AND whether they are one- or two-sided *Only common tests should be described solely by name; describe more complex techniques in the Methods section.*
☐	☒ A description of all covariates tested
☐	☒ A description of any assumptions or corrections, such as tests of normality and adjustment for multiple comparisons
☐	☒ A full description of the statistical parameters including central tendency (e.g. means) or other basic estimates (e.g. regression coefficient) AND variation (e.g. standard deviation) or associated estimates of uncertainty (e.g. confidence intervals)
☐	☒ For null hypothesis testing, the test statistic (e.g. *F*, *t*, *r*) with confidence intervals, effect sizes, degrees of freedom and *P* value noted *Give P values as exact values whenever suitable.*
☒	☐ For Bayesian analysis, information on the choice of priors and Markov chain Monte Carlo settings
☒	☐ For hierarchical and complex designs, identification of the appropriate level for tests and full reporting of outcomes
☐	☒ Estimates of effect sizes (e.g. Cohen's *d*, Pearson's *r*), indicating how they were calculated

Our web collection on statistics for biologists contains articles on many of the points above.

Software and code

Policy information about availability of computer code

Data collection	Immunohistochemistry images were analysed with HALO 10 software (IndicaLab). Immunofluorescence data were obtained with AxioScan (Zeiss)
Data analysis	Data was analysed with R software (version 3.4.4) and packages gplots, survival and FactoMineR. Custom code was produced in R for the analysis.

For manuscripts utilizing custom algorithms or software that are central to the research but not yet described in published literature, software must be made available to editors/reviewers. We strongly encourage code deposition in a community repository (e.g. GitHub). See the Nature Research guidelines for submitting code & software for further information.

Data

Policy information about availability of data

All manuscripts must include a data availability statement. This statement should provide the following information, where applicable:

- Accession codes, unique identifiers, or web links for publicly available datasets
- A list of figures that have associated raw data
- A description of any restrictions on data availability

The transcriptomic datasets analysed in this study can be accessed on the GDC Portal (TCGA SARC) and the Gene Expression Omnibus repository (accession numbers GSE21050, GSE21122, GSE30929). Immunohistochemistry, gene expression and clinical-related to NTUH cohorts (Fig. 3, Extended Data Figs. 7 and 8) are available from the corresponding author on reasonable request. The data that support the findings related to Fig. 4 are available from SARC but restrictions apply to the availability of these data, which were used under license for the study. Data are however available upon reasonable request to HAT (HTawbi@mdanderson.org) and with permission of SARC. All code used in this study is available from the authors upon reasonable request.

Field-specific reporting

Please select the one below that is the best fit for your research. If you are not sure, read the appropriate sections before making your selection.

☒ Life sciences ☐ Behavioural & social sciences ☐ Ecological, evolutionary & environmental sciences

For a reference copy of the document with all sections, see nature.com/documents/nr-reporting-summary-flat.pdf

Life sciences study design

All studies must disclose on these points even when the disclosure is negative.

Sample size	TCGA SARC: n=213, GSE21050: n=283, GSE21122: n=72, GSE30929: n=40, FSG: n=168, NTUH n=93, SARC028: n=47. Total: n=916.
Data exclusions	20 tumours from the NTUH cohort were excluded from gene expression (end SIC) analysis due to low quality of the extracted RNA.
Replication	No replication was done, but validation cohorts were analysed.
Randomization	Randomization is only relevant to the SARC028 cohort, which was previously published.
Blinding	All image and data analysis were performed blindly, independently of sample knowledge.

Reporting for specific materials, systems and methods

We require information from authors about some types of materials, experimental systems and methods used in many studies. Here, indicate whether each material, system or method listed is relevant to your study. If you are not sure if a list item applies to your research, read the appropriate section before selecting a response.

Materials & experimental systems

n/a	Involved in the study
☐	☒ Antibodies
☒	☐ Eukaryotic cell lines
☒	☐ Palaeontology
☒	☐ Animals and other organisms
☐	☒ Human research participants
☒	☐ Clinical data

Methods

n/a	Involved in the study
☒	☐ ChIP-seq
☒	☐ Flow cytometry
☒	☐ MRI-based neuroimaging

Antibodies

Antibodies used	CD3: 2GV6, Roche ; DC-Lamp: 1010E1.01, Dendritics ; CD20: L26, AGilent ; CD8: C8/144B, Agilent ; CD21 : 1F8, Agilent ; CD23 : SP23, Abcam; CD34: Qbend-10, Agilent ; PD-L1: E1L3N, Cell Signaling ; PD-1: EH33, CoStim Pharmaceuticals ; .
Validation	The specificity of anti-CD3, anti-CD4, anti-CD8, anti-CD20, anti-CD21, anti-CD23, anti-CD34, anti-CXCR5 and anti-DC-Lamp antibodies, and MECA-79 (PNAd) was validated on FFPE tonsil sections as positive control. For anti-CD20, certified manufacturing facilities from the company guarantee full quality control including western blot and studies using COS-1 cells transfected with cDNA encoding the CD20 molecule indicate that the antibody labels an intracytoplasmic epitope localized on the CD20 molecule. For anti-CD8, certified manufacturing facilities from the company guarantee full quality control including western blot and indicate that the antibody recognizes the cd8alpha chain. For anti-CD34, certified manufacturing facilities from the company guarantee full quality control. For anti-CD21, certified manufacturing facilities from the company guarantee full quality control including western blotting of the immunogen, and that the antibody labels cells or cell lines known to express CD21 (Raji, NC 37, tonsil cells), whereas no labeling is observed in the CD21-negative Jurkat cells (T-cell line) and human erythrocytes. For anti-CD23, certified manufacturing facilities from the company guarantee full quality control including western blotting, IHC on human tonsils and flow cytometry on Raji cells. For anti-CXCR5, certified manusfacturing facilities from the company guarantee full quality control using human CXCR5 transfectants by flow cytometry and lack of cross reactivity with human CXCR2, CXCR3, or CXCR4 transfectants. For PNAd, certified manufacturing facilities from the company guarantee full quality control including western blotting, IHC and flow cytometry. For anti-PD-L1, specificity was validated by the company using immunohistochemical analysis of paraffin-embedded human placenta using PD-L1 (E1L3N®) XP® Rabbit mAb in the presence of control peptide or antigen-specific peptide. Specificity was verified by using FPE sections from placenta as positive control and cerebral cortex tissue as negative control. Anti-PD-1 (Freeman GJ and col.) was obtained from CoStim Pharmaceuticals and validated as described in Fig. S1 of Giraldo et al., Clinical Cancer Research, 2015. Tonsil, placenta and cerebral cortex slides were obtained from Geneticist Inc.

Human research participants

Policy information about studies involving human research participants

Population characteristics	All available characteristics are reported in Extended Data Table 1.
Recruitment	Patients were recruited prior to the study and were not selected on specific criteria other than their pathology.
Ethics oversight	The research was approved by the Research Ethics Committee of NTUH (201605061RINA).

Note that full information on the approval of the study protocol must also be provided in the manuscript.